TRANSFER PRINTED SEMICONDUCTOR NANOMEMBRANES FOR

HETEROGENEOUSLY INTEGRATED MULTI-BAND IMAGER ARRAYS

by

LAXMY MENON

Presented to the Faculty of the Graduate School of

The University of Texas at Arlington in Partial Fulfillment

of the Requirements

for the Degree of

DOCTOR OF PHILOSOPHY

THE UNIVERSITY OF TEXAS AT ARLINGTON

May 2016

April 08, 2016

Abstract

TRANSFER PRINTED SEMICONDUCTOR NANOMEMBRANES FOR
HETEROGENEOUSLY INTEGRATED MULTI-BAND IMAGER ARRAYS

Laxmy Menon PhD

The University of Texas at Arlington, 2016

Supervising Professor: Name WEIDONG ZHOU

The electronics industry is ruled by silicon which is realized as the solution to meet the requirements of higher bandwidth and low cost high density monolithic integration. However, silicon has its limitations when it comes to high frequency or optoelectronic applications. Fusion of several functionalities on one chip can be obtained by heterogeneous integration of materials that have optimized performance for a specific application. The ability to tailor heterogeneous materials to be able to integrate them with each other, in rigid or flexible form, can lead to novel and superior functionalities, with impact in multitude of areas like electronics, optoelectronics, spintronics, biosensing and photovoltaics. Imaging systems benefit highly from integrating materials with different bandgaps, which in turn leads to detection in several wavelength ranges. Multi-band and multispectral imaging has various applications in remote sensing, industrial surveillance systems, bio photonics, automotive cameras, fluorescent imaging, spectrometer on a chip, LADAR and free space optical communications. The aim of this thesis is to explore various materials, configurations and integration schemes for efficient photodetection in several wavelength bands, and to achieve this with low cost, less bulky substrates, and easy fabrication techniques. The predictions of performance and efficiency for the structure and designs employed for various configurations are validated by measurement results and performance analysis after fabrication.

To realize a photodetector in visible wavelength band, silicon is the most widely used material. With its bandgap of 1.1 eV, silicon can cover a wide range of wavelengths from 400nm to 1.1 μm. An 8x8 array of silicon photodetectors is first demonstrated, with characterization results. The structure and thickness of each layer in the silicon active region is optimized to obtain maximum absorption and hence high photo response in the blue, green and red wavelengths. The rejection ratio or the ability of each P-N junction to have maximum responsivity to a specific wavelength compared to the others is measured. By the process of membrane transfer, silicon active layer is transferred to a kapton substrate, enabling flexibility and bending. The 8x8 Si PD array is fabricated on the kapton substrate, and the performance is analyzed and compared with that of a Si PD array on rigid silicon substrate.

InGaAs is one of the materials that can be used to detect the Near IR wavelengths due to its bandgap of 0.75 eV. InGaAs PDs have high responsivity, low power consumption and lower dark currents. InGaAs detector fabrication is explored to cover detection in the near IR wavelength range. Initially, the fabrication of a single detector is described, with measurement results of responsivity to IR wavelengths. This paves way for InGaAs 8x8 photodetector array, which is first fabricated on rigid substrate. Photoresponse to 980 nm and 1550 nm lasers are investigated, and responsivities are measured. InGaAs photodetector array on flexible substrate is investigated next. The InGaAs photodetector array is fabricated on InP substrate and then transferred to kapton by black wax transfer method. Performance comparison is made before and after transfer of the PD array to kapton.

Different heterointegration techniques and architectures are investigated to combine Si and InGaAs to form a detector capable of detection in visible and Near IR regime. Vertical integration of Si on InGaAs reduces the real estate but has more

fabrication complications as compared to adjacent integration. Both the layouts are explored in detail. A new method of transferring unconnected silicon mesas from the SOI substrate to the InGaAs substrate is proposed and investigated in detail. This technique of transferring Si mesas allows for an aligned transfer and can be extended to any materials.

Table of Contents

List of Illustrations

x

List of Tables

Chapter 1

INTRODUCTION

1.1 Motivation

Silicon has dominated the integrated electronics industry since John Bardeen, William Shockley and Walter Brattain demonstrated in 1947 that the flow of electricity through silicon can be effectively controlled. Silicon wafers are heavily used in the semiconductor industry to make transistors, solar cells, detectors, Raman lasers etc. Silicon can be effectively utilized to detect visible radiation due to its bandgap of 1.1um. Common approaches in place today involve color discrimination based on optical filters with relatively slow refresh rate or compromised spatial resolutions. There have been several efforts made to stray away from the commonly used optical sensing with Color Filter Arrays (CFA), as they suffer from color aliasing effects (color moiré effect). Several layouts of silicon have been explored to separate the color information of visible spectrum, like PIN, PINIP,NIPIN, PININIP,NIPIIN, TCO/PINIP/TCO/PIN, with different materials, biasing, configurations and illumination conditions. Vertically integrated structure, where the absorption of photons occur at different depths, depending on the wavelength of the incident light, can avoid the inevitable transmission loss, color aliasing effect and resolution limitation encountered with color filter array(CFA) based sensor arrays.

Heterogeneous integration is realized as a promising approach to build high performance photonic devices. Heterogeneous integration of III V devices with CMOS has enabled combining the extensive optical capabilities of III V materials with the mature CMOS industry. Since the bandgap of silicon limits the wavelength of detection to 1.1um, it is necessary to use another material like InGaAs, with a bandgap of 0.75eV, to detect NIR.

Another motivation is thin film electronics and more recently, nanomembranes for integrated and flexible silicon photonics. Remarkable progress has been made in the field of thin film electronics starting from thin film silicon solar cells in 1960s to the mode sophisticated large area thin film displays. A variety of stretchable, foldable and transfer printed ultra-thin silicon integrated circuits have been demonstrated with the use of flexible silicon nanomembrane.

1.2 Overview of dissertation

Chapter 2 begins with presenting an introduction to InGaAs photodetector. Background of InGaAs photodetector is discussed, followed by fabrication details of a single InGaAs photodetector. Then, the fabrication details for a 8* 8 InGaAs array is discussed, followed by IV test results. The InGaAs array was then transferred to a flexible kapton substrate, and the details of this process are described, with fabrication steps, and characterization results.

Chapter 3 presents the design simulation, fabrication and characterization results of a flexible silicon 8*8 array. Silicon photodetector array on rigid substrate is first analyzed, with the optimized structure design and simulation results from Medici. Consequently, silicon photodetector array on flexible substrate is demonstrated with detailed description of the fabrication steps and characterization results. The experimental results are compared with the values predicted by simulation. Comparison between dark currents before and after transfer is performed to check the efficiency of transfer. Flexibility tests are demonstrated and the performance of the array under bent state is investigated by comparing the IV performance before and during bent state.

Chapter 4 analyzes one of the heterogeneous configurations of Si and InGaAs, which is vertically stacking InGaAs membrane on Si substrate. All the process details, from transfer to final interconnect step is discussed, along with the characterization results, to show good isolation between Si and InGaAs. Comparison between illumination with visible and IR wavelengths is made, and the performance of Si and InGaAs is compared with each illumination.

Chapter 5 investigates the adjacent placement of Si and InGaAs for heterogeneous integration. The structure and fabrication challenges are explained, with a

novel method of transfer of silicon mesas to InGaAs, with alignment to achieve heterogeneous integration by lateral alignment of silicon and InGaAs photodetectors.

Chapter 2

InGaAs Photodetector

2.1 Background

People have tried various means to detect and analyze infrared radiation in sunlight, that is invisible to the naked eye, ever since Friedrick William Herschel discovered this spectrum of light in the early 19th century[1]. The earliest practical IR detectors were developed by Macedonio Melloni in the mid-19th century which relied on the differences in thermal expansion of two dissimilar metals and were basically thermopiles that functioned by thermal conduction[2]. Infrared is the portion of the electromagnetic spectrum that lies between the visible light and microwaves. This spectrum ranges from 700nm to about 1mm, which equates to a frequency range of 1 THz and 300 GHz. Fig 2-1 shows the electromagnetic spectrum comprising of the infrared band. As can be seen, the infrared band consists of short-wave IR, Medium-wave IR and long-wave IR. Each band has its own characteristics and applications.
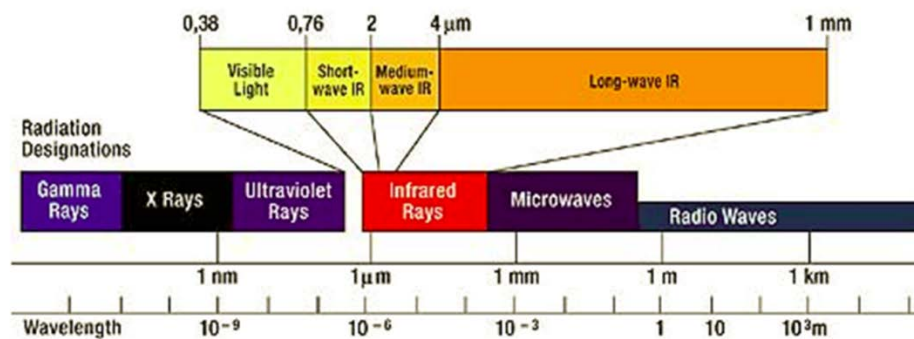
Figure 2-1 Electromagnetic spectrum

Infrared detectors convert IR radiation into electrical signals. Infrared detectors have been used to detect measure and image thermal radiation since the 1940s (1). IR

5

detector technology was developed and is continued to be driven primarily by military applications. New materials and technology has expanded its use and applications in the civilian sphere as well. Infrared detectors are usually used in a Focal Plane Array (FPA) layout to detect more photons, where the individual detector elements are assembled at the focal plane of an imaging system. Many types of IR detectors are used in FPAs, like photon and thermal detectors that address a wide variety of requirements. Several intrinsic and extrinsic detectors are used to detect IR radiation. HgCdTe(MCT) and InSb are the most common intrinsic detectors. The main disadvantage of MCT is that dark currents in MCT devices tend to be extremely large, much larger than in other devices like InGaAs, influenced heavily by band-to-band tunneling[3, 4]. Precision growths of MCT extremely difficult due to issues like differences in the densities and melting points of the constituent materials, the relative softness of the final material, and a number of crystalline properties of the material like high interdiffusion coefficients, low bond strength, and a high rate of dislocation formation[5-7]. Finely controlling the composition of materials is difficult as the bandgap decreases. Variation of the mole composition of MCT by 0.001 can have drastic effects on the performance of a detector as the band gap goes down towards the LWIR and VLWIR regimes. MCTs suitability for some applications is also questionable as it is difficult to achieve uniformity across the wafer, which is essential for focal plane arrays [4, 6, 8]. The use of InSb for photodetectors has been associated with a number of fabrication difficulties like strict tolerances in terms of lattice matching to a substrate. When attempts were made to utilize the common substrates like GaAs or Si, the InSb/substrate interface suffered from high dislocation densities despite the use of a number of advanced techniques (e.g., inclusion of buffer layers) to ease the strain which in turn led to large leakage currents, and hence lower detectivities[9]. When operating at low temperatures, which is necessary due to dark

6

current considerations, the response that InSb materials have in the LWIR regime is further reduced[5].Other materials like PtSi, InGaAs, Ge, InGaAs/InP, are also used[10]. The applications of IR detectors are several, for example IR astronomy, IR spectroscopy, global monitoring of environmental pollution, chemical process monitoring, IR imaging, car driving, long time prognosis of crop yield, radiation analyzers, remote sensing, systems for recognition and surveillance, tank sight systems, anti-tank missiles, air-air missiles (3,4). Different types of detectors can be combined with readout circuits in a hybrid configuration to form detector arrays in several such applications.

Detector systems based on InGaAs have spectral response from 0.9 μm to 1.7 μm .Most detectors are formed in MOCVD grown $In_{0.53}Ga_{0.47}As$, lattice matched to InP substrate. The detection can be extended to the visible range by removing the InP substrate[11, 12]. InGaAs is widely preferred as the material for Near IR(NIR) detection due to its low dark current, excellent uniformity, mature fabrication technology, low production cost and operation at or near room temperature using thermoelectric cooling[13]. Several groups and companies have built large area InGaAs focal plane arrays for various applications like low level light imaging, day/night vision imager, astronomy, dense wave division multiplexing (DWDM) systems and NIR imaging[11, 12, 14-20]. Both planar [21-25] and mesa structures [26-29] have been explored for fabrication of the InGaAs detectors. Mesa structures have low thermally stimulated leakage and low leakage from conduction from surface states. They also have better stability of dark current when compared to mesa etched structures[21]. However, my work will focus on mesa etched InGaAs PIN photodetectors, as they are easy to fabricate and have low capacitance, in order to achieve high bandwidth low-noise receiver operation.

Over the years, a large number of metrics have been developed to measure the performance of IRPDs. For single pixel detectors, the most common metrics are dark current density, peak detectivity , peak responsivity, and operating temperature. Lower dark current densities allow lower response signals to be detected, a desired trait in all devices. Comparisons of dark currents at a given temperature within a single technology are a valid means of determining superior performance[30]. All of my devices are tested at room temperature and other units of merit will be discussed in the characterization section.

My work is focused on building a flexible InGaAs array, which can have wider applications in the field of NIR imaging, and flexible photonics. This flexible InGaAs array will be a stepping stone to build heterogeneously integrated Si/InGaAs array.

2.2 Single InGaAs PD on substrate

2.2.1 Introduction

The structure of the InGaAs used is PIN, with 2 μm I layer. A PIN structure has high responsivity and is better suited for high bandwidth applications, when compared to a PN diode. They are also less expensive and consume less voltage than avalanche PDs. There are two sacrificial layers for etch stop after the PIN layers, as shown in table 2-1. The operating principle of the InGaAs PD, is that when light enters the active area of a PIN photodetector, the photons are absorbed by the I layer. The electrons in the PD are excited and pulled to the conduction band from the valence band, thus generating electron hole pairs. The photogenerated carriers are accelerated in the opposite directions by the applied reverse bias, which gives rise to photocurrent. The magnitude of photocurrent depends on the quantum efficiency of the device.

8

Table 2-1 Structure of the InGaAs PIN used for fabrication

Layer No.	Description	Material	Thickness	Dopant	Doping
5		$In_{0.53}Ga_{0.47}As$	50 nm	p	1e19 cm^{-3}
4		$In_{0.53}Ga_{0.47}As$	2000 nm	i	UID
3		$In_{0.53}Ga_{0.47}As$	300 nm	n	1e19 cm^{-3}
2	Sacrificial	InP	150 nm	Si	5e18cm-3
1	Sacrificial	$In_{0.53}Ga_{0.47}As$	150 nm	Si	5e18cm-3
S.I. InP Substrate					

The values of responsivity and efficiency for the InGaAs detector structure in table 2-1 is simulated with Taurus Medici software and shown in figure 2-2.
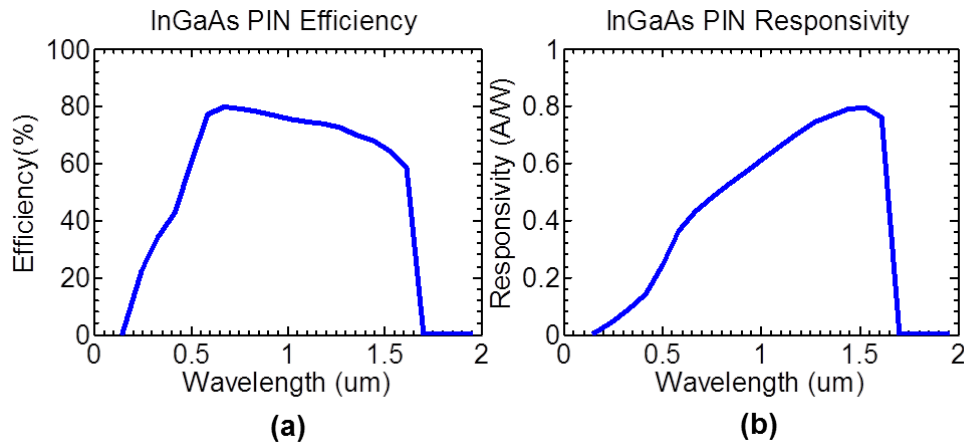
Figure 2-2 Simulated values of (a) responsivity and (b) efficiency for the structure in Table 2-1

9
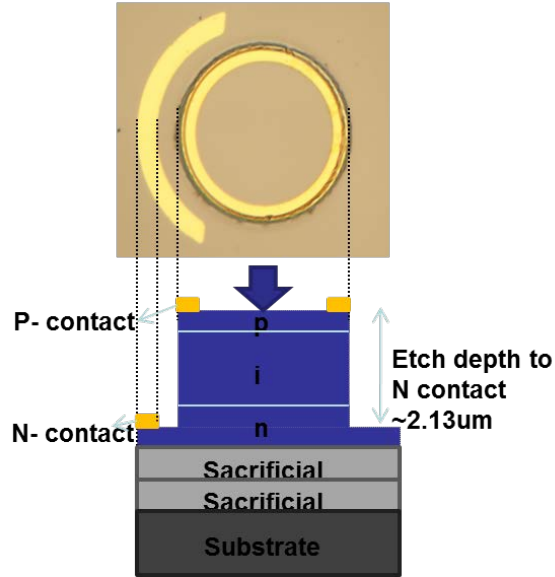
2.2.2 Fabrication

Figure 2-3 Completed single InGaAs PD with schematic of the structure.

The completed single InGaAs photodetector on InP substrate is shown in figure 2-2. The fabrication process begins with first defining the P contact ring by photolithography using a negative photoresist. The P contact ring metal is done by e-beam evaporator. The P metal used is Pd/Zn/Pd/Au. P mesa is then defined by photolithography, and mesa etching is done in by wet etching with $HF+H_2O_2+H_2O$ (1:1:10) to a depth of 2.13 μm. Once the mesas are etched, the n metal contact area is defined by photolithography again, and contact metal is deposited in an e-beam evaporator. The n contact metals used are Ni/Ge/Au/Ti/Au.

2.2.3 Characterization-IV

One of the important units of merit for photodetector is its responsivity, which is defined as the ratio of the output current to the input optical power. To determine the

performance of the InGaAs photodetector, the PD was illuminated with 980 nm laser, and the response of the PD to increasing intensities of the laser was recorded, for the voltage range of -2V to +2V. The resulting plots are shown in Figure 2-3 (a). The input power vs. output current and responsivity is also shown in Figure 2-3(b, c), for various values of bias.
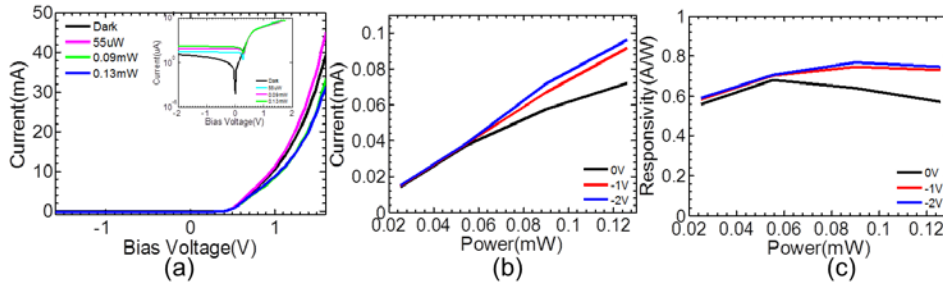
Figure 2-4 (a) IV characteristics- Response of the PD to increasing intensity of 1550nm laser (b) Power Vs current characteristics and (c) Power vs responsivity characteristics.

2.3 InGaAs PD array

2.3.1 Introduction

After fabrication and characterization of a single device, the next endeavor was the fabrication of an 8x8 InGaAs PD array. The array of InGaAs pixels is also called focal plane array (FPA) as they will be arranged in the focal plane of a lens. FPAs operate by detecting photons at particular wavelengths and then generating an electrical charge, voltage, or resistance in relation to the number of photons detected at each pixel. The structure of InGaAs used for the InGaAs PD array is same as that for single InGaAs PD device, except the thickness of P and N layers.

Table 2-2 Structure of InGaAs used for fabrication

Layer No.	Description	Material	Thickness	Dopant	Doping
5		$In_{0.53}Ga_{0.47}As$	50 nm	p	$1e19\ cm^{-3}$
4		$In_{0.53}Ga_{0.47}As$	2000 nm	i	UID
3		$In_{0.53}Ga_{0.47}As$	300 nm	n	$1e19\ cm^{-3}$
2	Sacrificial	InP	150 nm	Si	5e18cm-3
1	Sacrificial	$In_{0.53}Ga_{0.47}As$	150 nm	Si	5e18cm-3
S.I. InP Substrate					

The responsivity and efficiency of the structure in Table 2-2 is simulated again with Taurus Medici and the results are shown in figure 2-5.
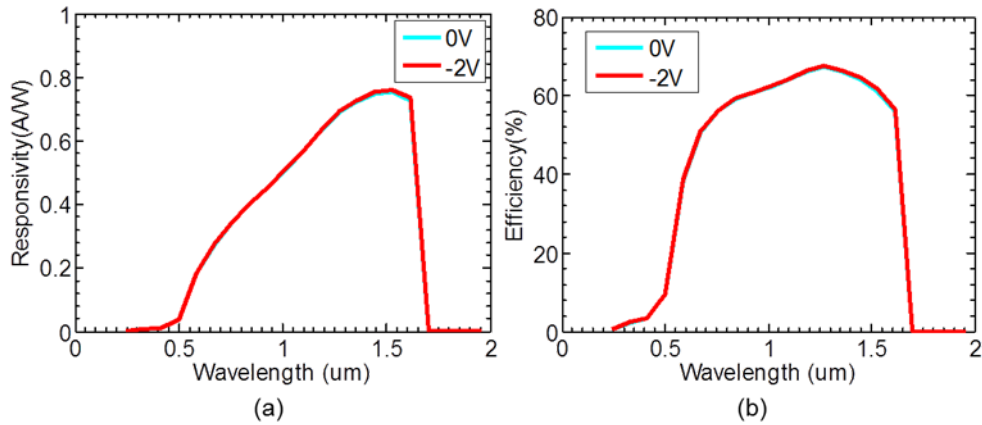
Figure 2-5 Simulated values of (a) responsivity and (b) efficiency for the structure in Table 2-2

2.3.2 Fabrication

Fabrication of the InGaAs 8x8 PD array begins with defining the P contact with photolithography. Pd/Zn/Pd/Au is used as the P contact metal and is deposited by e-beam evaporator. Next step is to etch the mesas to the InP substrate to isolate the pixels from each other. The mesa etching in done in a DRIE chamber, with BCl_3/Cl_2 gases, to a depth of 2.56 µm. Since photoresist doesn't survive in the etch chamber with this etch

chemistry, SiO2 is used as the mask. Once the mesas are defined, n contact region has to be defined by etching a 20x20μm area to a depth of about 2.2 μm. The next step is to pattern for the N contact, followed by deposition of the N contact metal by e-beam evaporation. It is necessary to deposit interconnect metal, to avoid damage to the mesas during characterization, and to enable wire bonding at a later step. The interconnect for the lower N contact is first deposited by e beam evaporator with the metals Cr/Au. This is followed by deposition of an insulating layer of HD4104 polyimide. Finally the interconnect for the top P contact is deposited on top of the polyimide. The completed device array is shown in figure 2-6. Figure 2-6 (a) and 2-6 (b) shows the SEMS of the 8x8 InGaAs PD array and single InGaAs PD respectively. Figure 2-6 (c) shows the optical image of the 8x8 InGaAs array. 8 PDs in a row share the same p interconnect pad, and the 8 PDs in a column share the same n interconnect pad. This leaves behind 16 metal pads, 8 lines/pads for the P interconnect, and 8 lines/pads for the N interconnect.

(a)	(b)	(c)
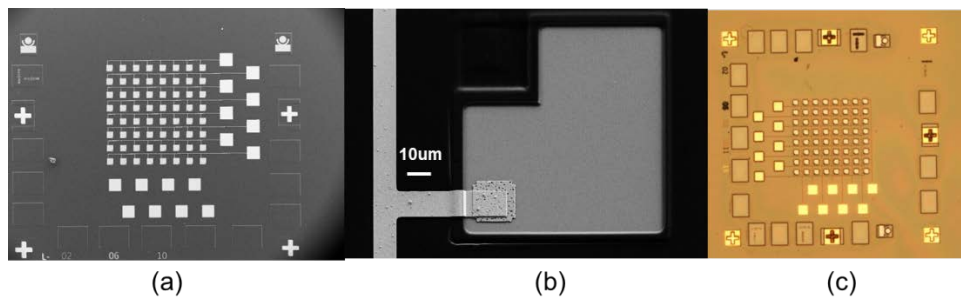
Figure 2-6 (a) SEM of the fabricated 8x8 InGaAs PD array (b) SEM of a single PD in the 8x8 array (c) Optical image of the 8x8 InGaAs PD array

2.3.3 Characterization- IV

To analyze the performance of the 8x8 PD array, all the 64 devices were tested individually for dark current and IV characteristics. The devices were kept in dark, and the

p and n contact metal of the pixels were probed, and the dark currents were recorded for a voltage range of -2 to +2 V. All the 64 devices are functional and their dark currents are shown in Figure 2-7. All the 64 devices in the array have uniform dark current values, and so we can expect a uniform photoresponse from all of the devices when they are illuminated with IR wavelengths.
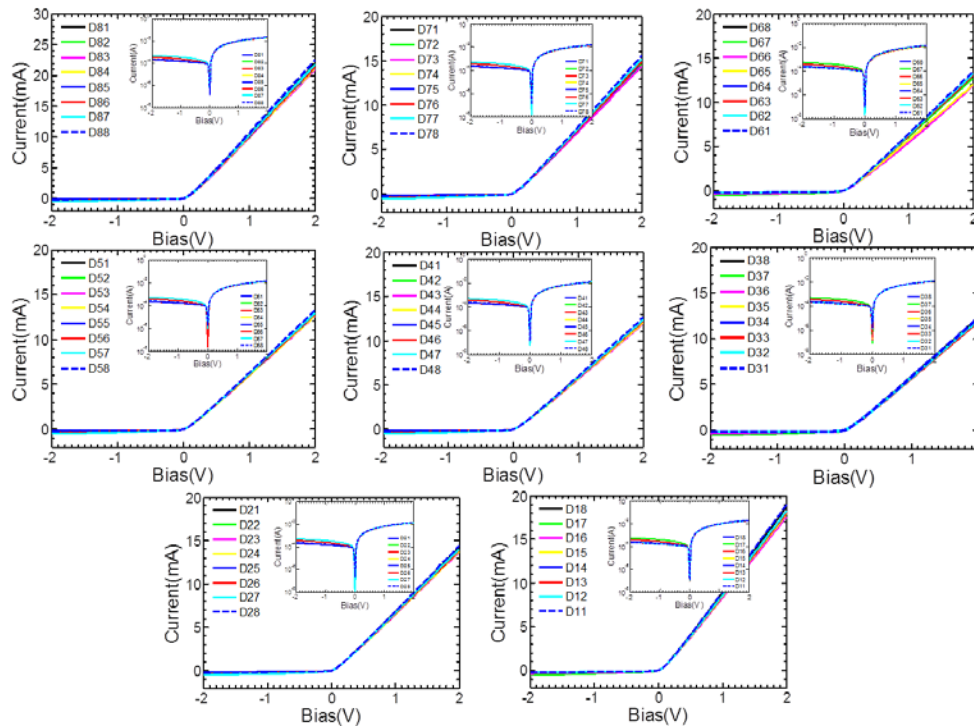
Figure 2-7 IV plots for all the 64 devices in the 8X8 array, shown in linear and log scale.

The devices were also tested for their photoresponse, by illuminating them with 980nm laser and 1550 nm laser. The devices were illuminated through a light wave probe to focus the light on the active region on the mesa. The lightwave probe has a 50um diameter ball lens at the tip, and he height is adjusted to focus maximum light on the specific device being tested. The intensity of the laser is varied and the response of the

device to each intensity is recorded. As can be seen from figure 2-8, the photoresponse of the device increases as the input intensity of the laser is increased. Output current vs. input power and responsivity vs. input power characteristics for various values of input bias are also investigated and shown in figure 2-8, for both 980nm and 1550nm laser illuminations.
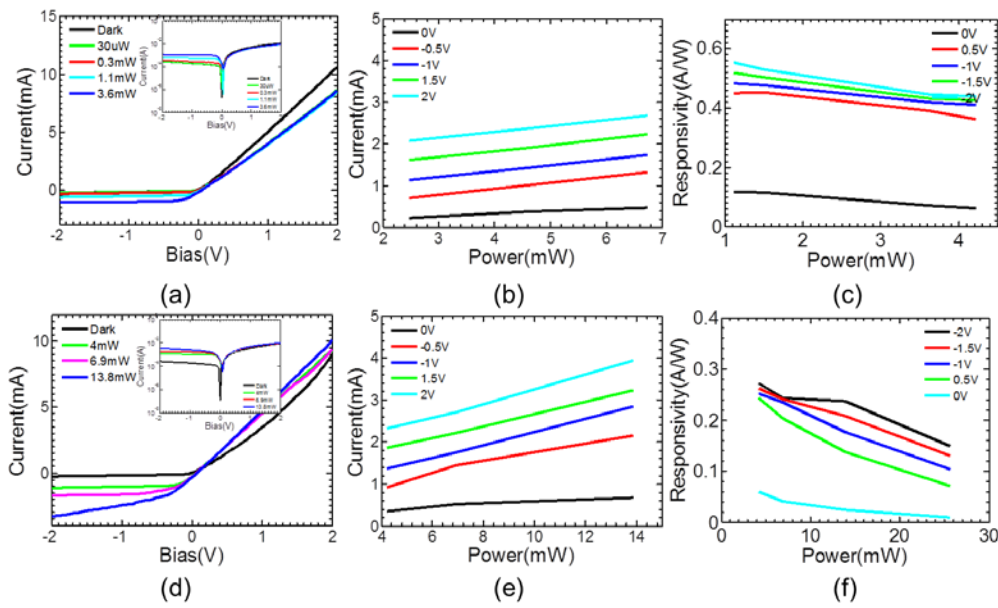
Figure 2-8 Characterization results with 980 nm laser and 1550 nm laser.(a) Response of the PD to increasing intensities of 980nm laser (b) Current vs. power characteristics for various voltage values for 980nm laser excitation (c) Responsivity vs. power plot for various voltage values for 980 nm laser. (d) Response of the PD to increasing intensities of 1550 nm laser (e) Current vs. power characteristics for various voltage values for 1550nm laser excitation (f) Responsivity vs. power plot for various voltage values for 980nm laser

The calculation of responsivity is done as the ratio of the output current of the mesa/pixel to the input laser power. The active region on the mesa, that can absorb photons and the area of the mesa illuminated by the laser is taken into account during the calculation of responsivity. A comparison between the simulated values of responsivity and the measured values of responsivity for both 980 nm and 1550nm laser inputs is done, and the results are summarized in figure 2-9. The simulation was done with Taurus Medici software .The comparison shows very good agreement between the simulated and measured values of responsivity.
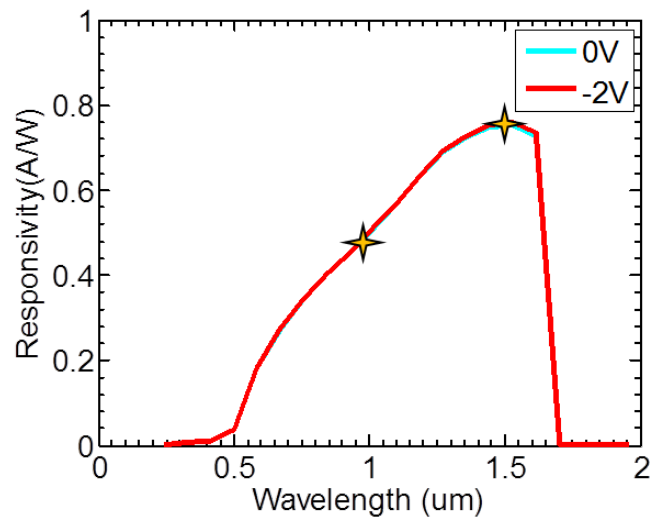
Figure 2-9 Comparison of simulated and measured values of responsivity

2.4 Flexible InGaAs PD array

2.4.1 Fabrication

The fabrication of the flexible InGaAs PD array begins with first fabrication of the PD array on InP substrate, and then etching away the substrate to transfer it to a flexible

substrate. InGaAs mesa and N contact region are etched using reactive ion etching, using BCl$_3$/Cl$_2$ chemistry, as shown in figure 2-10 (a). Hard mask (SiO$_2$) is used instead of photoresist because it offers better selectivity in the RIE chamber. The etch area is 36 μm x36 μm. P and N contact metals are deposited after photolithography using an e- beam evaporator. Bottom and top interconnects are the deposited with a passivating layer of polyimide in between as pictured in Fig 2-10 (b) and 2-10 (c). The mesa is 100 μm x100 μm and spaced 100 μm apart. An optical image of the completed array is shown in figure 2-11(a).

(a) (b)

(c)
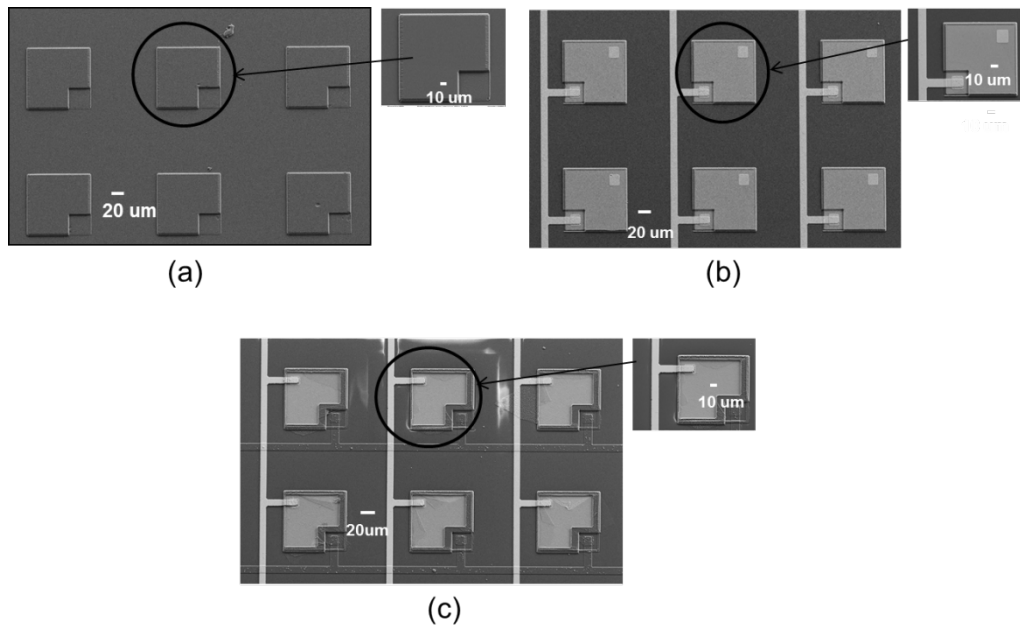
Figure 2-10 SEM images of device at various stages of processing (a) After N etch and mesa etch (b)After bottom interconnect (c) after polyimide and top interconnect

Once the PD array fabrication is completed on InP substrate, the top surface of the PD array is covered with black wax, to protect it from being etched , while the substrate is being etched. The device array covered with black wax is left to settle for

about 5- 6 hours before immersing it in a solution of HCl +H_3PO_4(1:4) to etch away the InP substrate. The etching of the substrate takes 3 hours. After this, the device layers remain and these layers , with the black wax is removed from the etchant solution and immersed in DI water. The kapton substrate is coated with SU-8 2 so that the membrane will have better adhesion to it. The PD array with the black wax is then placed on the SU-8 coated kapton. The black wax is then removed with Trichloroethylene (TCE). This leaves behind the InGaAs membrane with the PD array on the kapton substrate, as shown in figure 2-11 (b).

(a)   (b)
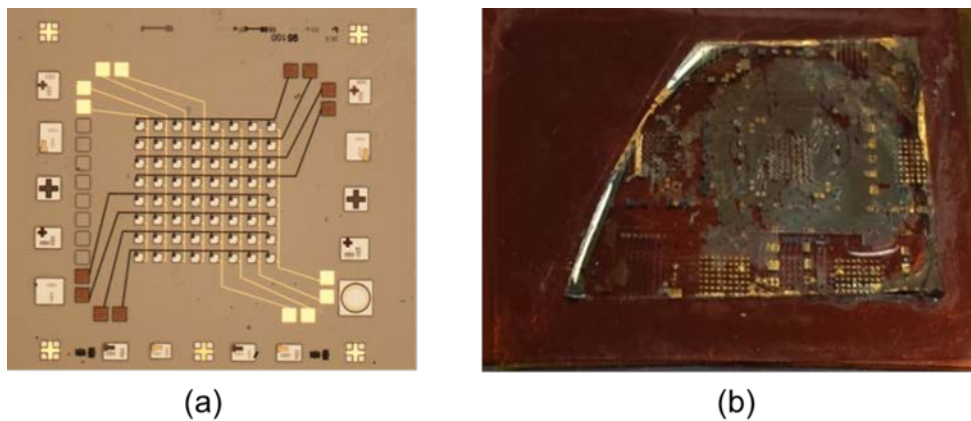
Figure 2-11 Optical images (a) After device completion on InP substrate (b)After transfer of the device array to kapton substrate.

2.4.2 Characterization- IV

IV measurements were performed before and after transfer to flexible kapton substrate to characterize the device, and compare the performance of the InGaAs PDs on rigid InP substrate and flexible kapton substrate. Figure 2-12 shows the photoresponse of the devices in the array, to increasing intensities of 980nm laser and 1550 nm laser. As expected, the response of the device increases when the intensity of the input laser is increased. The insets show the same IV plots in a log scale.

18
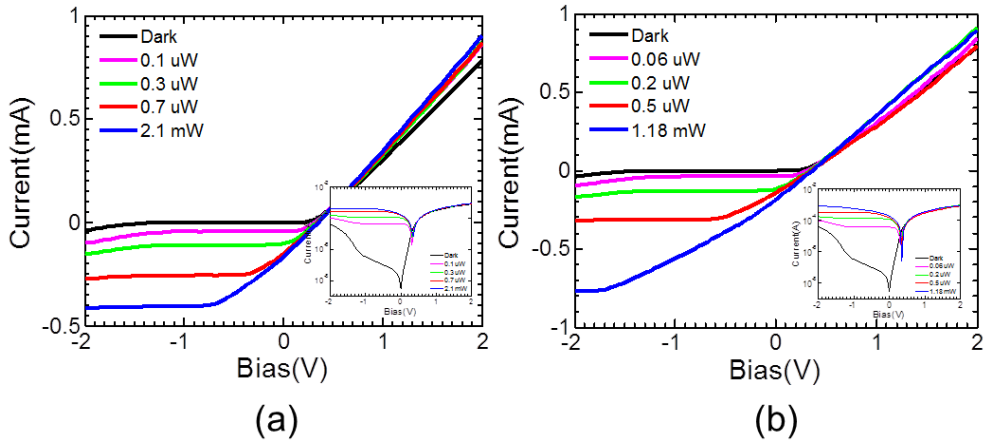
Figure 2-12 Response of the InGaAs PD array on kapton to increasing intensities of (a) 980 nm laser and (b) 1550nm laser.

Comparison between the response measurements before and after transfer to kapton shows some degradation in the photoresponse after transfer to kapton, as shown in figure 2-13.This degradation is caused due to uneven wet etching during the substrate removal and sacrificial layer removal steps. Another reason could be due to the residual black wax left behind after TCE clean. This reduction in responsivity can be improved by better control of wet etching depths, and by thorough rise with TCE during black wax removal, followed by a gentle acetone rinse.
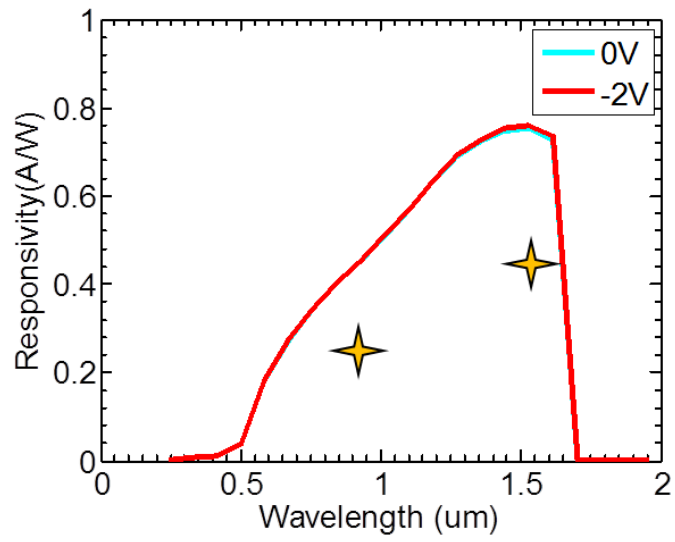
Figure 2-13 Comparison between simulated and measured values of responsivity of

InGaAs after transfer

Chapter 3

Silicon photodetectors

3.1 Background

Silicon is the eighth most common element in the universe by mass. Elemental silicon also has a large impact on the modern world economy. Although most free silicon is used in the steel refining, aluminum-casting, and fine chemical industries (often to make fumed silica), the relatively small portion of very highly purified silicon that is used in semiconductor electronics (< 10%) is perhaps even more critical. Due to the wide use of silicon in integrated circuits, the basis of most computers, a great deal of modern technology depends on it. pure silicon is doped with small concentrations of certain other elements, a process that greatly increases its conductivity and adjusts its electrical response by controlling the number and charge (positive or negative) of activated carriers. Such control is necessary for transistors, solar cells, semiconductor detectors and other semiconductor devices, which are used in the computer industry and other technical applications.

Visible wavelength spectrum, that the human eye is capable of seeing, is from 400-700nm, as shown in figure 3-1
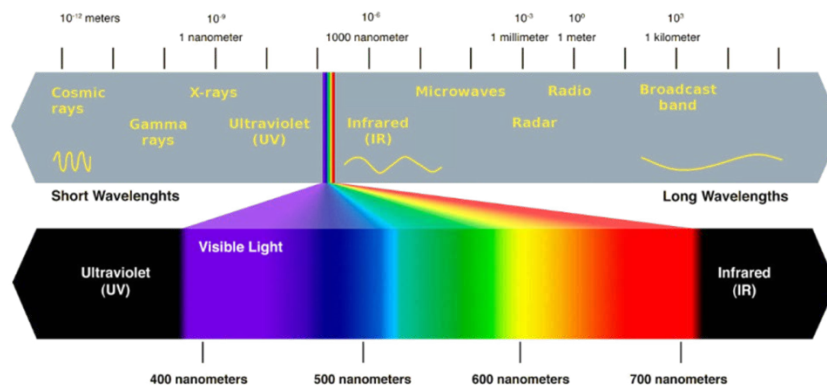
Figure 3-1 Visible wavelength range in the electromagnetic spectrum

Si photodetectors convert optical power into an electrical current . Due to a bandgap of 1.1 eV, Si PDs are mostly used as detectors for the visible range of wavelengths. Silicon multi-color photodetector (PD) arrays, capable of simultaneous sensing of light of multiple wavelengths by one pixel, are highly desirable for sensing and imaging applications. Common approaches in place today involve color discrimination based on optical filters with relatively slow refresh rate or compromised spatial resolutions. There have been several efforts made to stray away from the commonly used optical sensing with Color Filter Arrays (CFA)[31, 32], as they suffer from color aliasing effects (color moiré effect). Since three color filters are spatially arranged to form one color pixel, their resolution is limited. Hydrogenated amorphous Si was extensively used to make multi color photodetectors as they exhibit excellent photosensitive properties, with its spectral response suiting the sensitivity of the human eye much better than crystalline silicon[33-39]. Several structures like PINIP, NIPIN, PININIP, NIPIIN, TCO/PINIP/TCO/PIN, PIIIN, PIN, and NIN have been explored to obtain two and three color detection with different materials, biasing, configurations and illumination conditions[34-40]. Vertically integrated structure, where the absorption of photons occur at different depths, depending on the wavelength of the incident light, can avoid the inevitable transmission loss, color aliasing effect and resolution limitation encountered with color filter array(CFA) based sensor arrays[41-43]

3.2 Principle

In semiconductor materials, the absorption depth of photons varies with the energy of photons. Due to this variation in absorption coefficient, the absorption depth of silicon is different for different wavelength; the greater the wavelength of light incident

22

upon silicon, the deeper the light will penetrate into silicon before it is absorbed. As light enters device, it is absorbed and produce electron-hole pairs in proportion to the absorption coefficient, yielding much more charge carriers for short wavelengths than for long wavelength near silicon surface[41]. As the absorption depth of Si varies over several orders of magnitude over the visible range, this property can be utilized to build a multicolor detector, using silicon, by having several PN junctions stacked on top of each other[44-47].
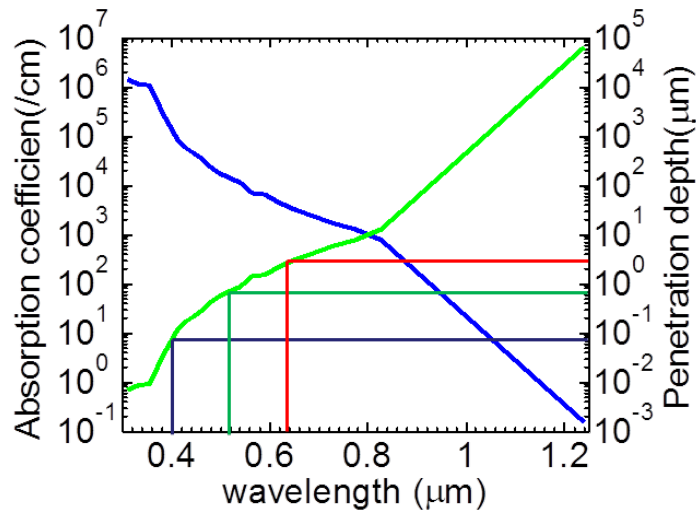
Figure 3-2 Variation of absorption coefficient and penetration depth with wavelength for silicon

It can be seen from the figure 3-2 that as the wavelength of incident radiation increases, penetration depth in silicon increases and absorption coefficient decreases. Due this property of silicon (and other semiconductor materials), the blue wavelength is absorbed on the surface or topmost layer, and red is absorbed at the deepest layer.

Keeping this in mind, if we were to design a vertical n-p-n-p structure in silicon, then, when illuminated with visible light, the blue wavelength is absorbed at the topmost PN junction, green wavelength is absorbed at the middle PN junction and red wavelength is absorbed at the bottommost PN junction, as shown in figure 3-3. The eye's cone cells have receptors, which allow the perception of low wavelength, medium wavelength and long wavelength radiations. The purpose of any imaging device is to duplicate an image as would be perceived by the eye. Once the three primary additive colors can be detected by the n-p-n-p structure, this method of photodetection can be utilized to recreate any image.
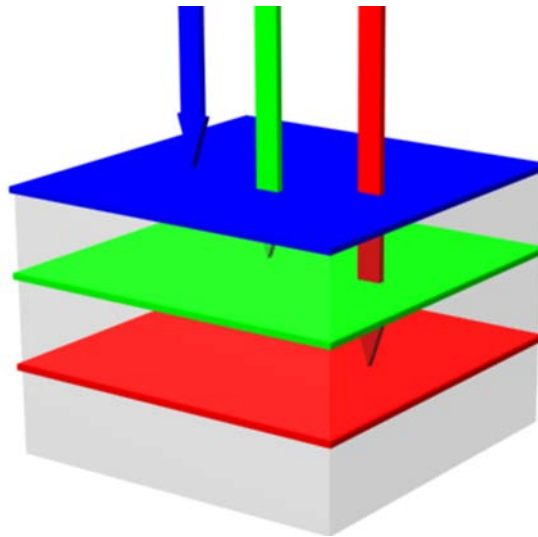
Figure 3-3 Absorption of blue, green and red wavelengths in a vertical NPNP

silicon structure

The NPNP structure and the layer thicknesses are designed keeping in mind the penetration depth of each wavelength in silicon, as per figure 3-2. The optimized SOI structure is shown in Table 3-1

Table 3-1 SOI structure of the multi-junction silicon for three color photodetection

Material	Thickness	Doping	Concentration
Si	0.2 µm	n+	$1E18 \, cm^{-3}$
Si	0.4 µm	p+	$1E18 \, cm^{-3}$
Si	1.4 µm	n+	$1E18 \, cm^{-3}$
Si	4.5 µm	p+	$1E18 \, cm^{-3}$
SiO_2 1.0 µm			
Si-substrate 660 µm			

To gauge the performance that can be expected from such a NPNP structure, simulations were performed with Taurus Medici software from Cadence. The simulation results for responsivity vs. wavelength and efficiency vs wavelength are shown in figure 3-4.
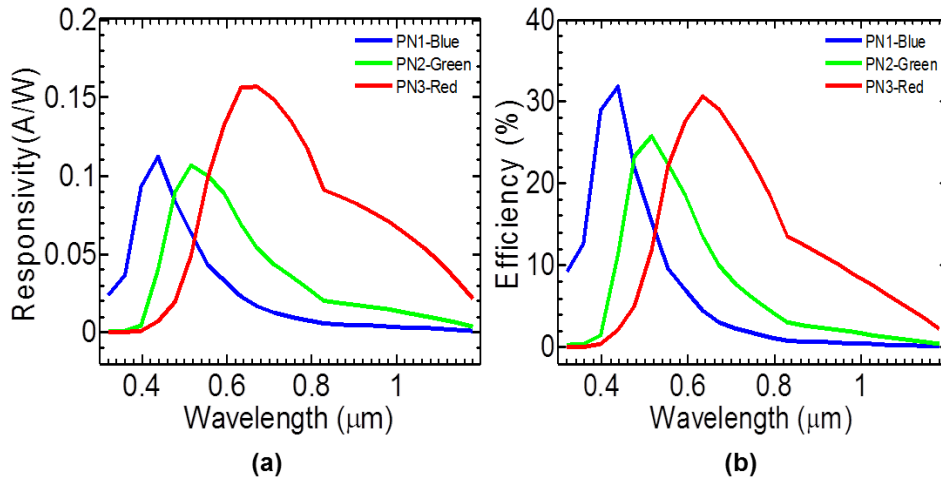
Figure 3-4 Simulation results of (a) Responsivity vs wavelength and (b) Efficiency vs. wavelength for blue, green and red P-N junctions in a three color silicon photodetector

Response of the three junctions to a 200n light s pulse is simulated, and shown in figure 3-5(a),(b) and (c). The rise time, fall time and bandwidth are also simulated for the three junctions and are shown in Figure 3-5(d), (e) and (f).
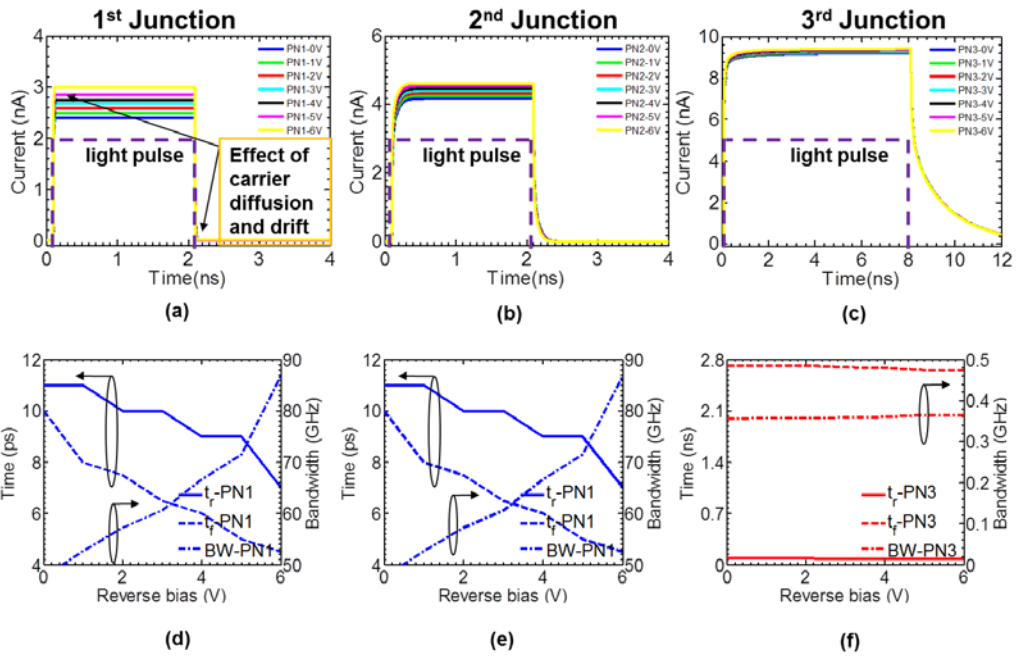
Figure 3-5 Simulation results (a,b,c) Response of junction1, junction2 and junction 3 to 200ns light pulse .(d,e,f) Rise time, fall time and bandwidth for junction 1, junction 2 and junction 3

3.3 Silicon PD array

3.3.1 Fabrication

(a)Etching contacts

(b)Metallization of contacts

(c)Pixel isolation

(d)Open pixels

(g)Top interconnect

(f)Polyimide Passivation

(e)Bottom interconnect
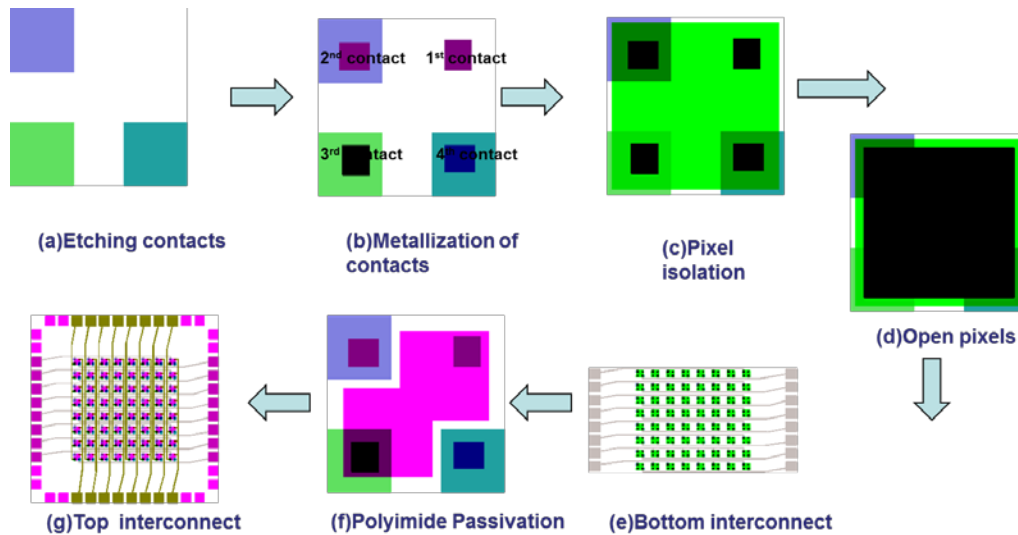
Figure 3-6 Schematic of the steps to fabricate silicon 8*8 array

The fabrication process begins with first defining the etch areas for the p and n contacts of the three junctions. This is done by photolithography using a Karl Suss Backside aligner, and NR9 photoresist. The top surface of the SOI layer is N doped and serves as one of the contact regions. The other p and n regions are defined by dry etching the SOI using a RIE etcher to 400 nm, 2.5 µm and 4.5 µm depths, using SF_6 gas [48]. The etched area is 36 µm x38 µm. Once the contact areas are exposed by etching, photolithography is done to define the metal contact regions to form a good ohmic contact with Si by metal deposition. Cr/Au is used as the contact metal, and is deposited by an e-beam evaporator. IV tests after this step confirms the existence of a good ohmic contact. After this, mesas are defined to isolate the pixels. A thick positive photoresist is needed, since

the Si active layer is 6.5 µm thick. The etching is done in a Trion DRIE etcher. After this step, all the 64 mesas are isolated from each other. Photolithography is then done with photo definable HD4104 polyimide, to provide the required height to connect the lower contacts with the lower interconnect layer. After polyimide curing at 250C for 2 hours, photolithography is done again to define the bottom two interconnect layers. This is followed by another polyimide passivation layer to electrically isolate the top and bottom interconnect layers. Finally, the top interconnects are deposited with an e-beam evaporator. The interconnect metals are Cr/Al/Cr/Au. The thickness of each passivation layer is adjusted to ensure good electrical connection between the local contacts and interconnect pads laid out above the polyimide. The optical images and SEMs of the device array at various stages of processing are shown in figure 3-7.
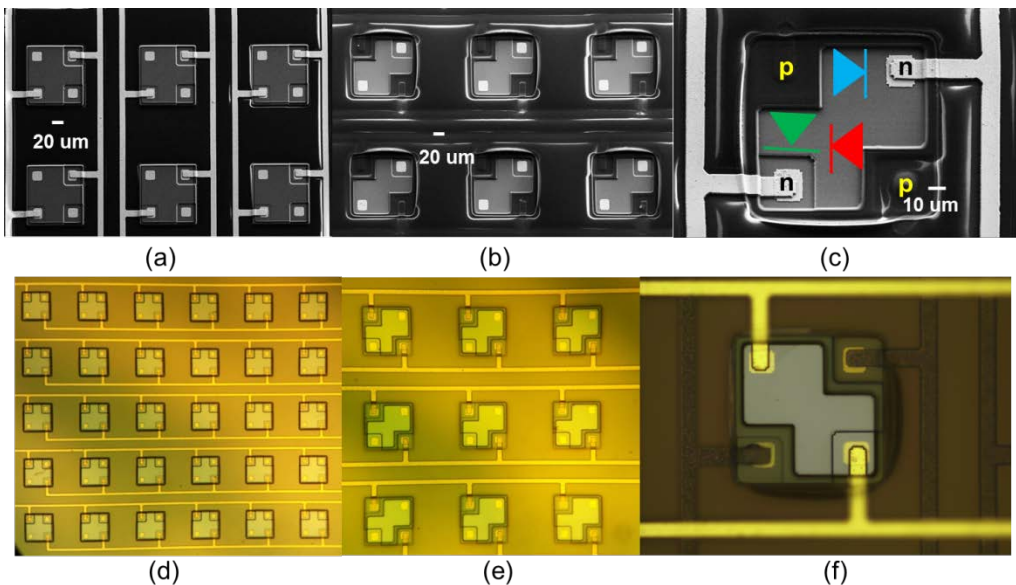
Figure 3-7 SEM and optical images at various stages of processing. SEM (a) after etching, with contacts and bottom interconnect pair (b) after polyimide passivation layer pattern (c) Zoom in of one pixel after top interconnect layer metal deposition

29

3.3.2 Characterization- Imaging

The performance of the fabricated 8x8 PD array is analyzed both with IV tests on the individual pixels and by imaging tests on the array. Figure 3- 7(a) shows the dark currents of junction 1, junction 2 and junction 3 for ne pixel in the array. All the pixels were checked for functionality and performance, and it was observed that the dark currents of all the devices for a specific junction were in the same range and hence uniform. The dark currents of all the devices for all the junctions were in the low nano ampere range. In figures 3-8 (b-d), the photo response of the specific junction is compared with that of dark current. In Figure 3-8 (b), the dark current of a pixel is compared with photoresponse to blue laser and white light, for junction 1. It is observed that the response to blue laser is two orders of magnitude higher than dark current, and response to white light, whose intensity is higher than blue laser, is three orders of magnitude higher than dark current. Similar comparison is made with junction 2 -green laser and junction 3- red laser. A trend similar to figure 3-8 (b) is observed in other cases too. All the pixels were tested for photoresponse in all the three junctions , and all the devices were found to be functional and following a similar pattern as that depicted here. The results of one pixel/device is shown here for the purpose of clarity.
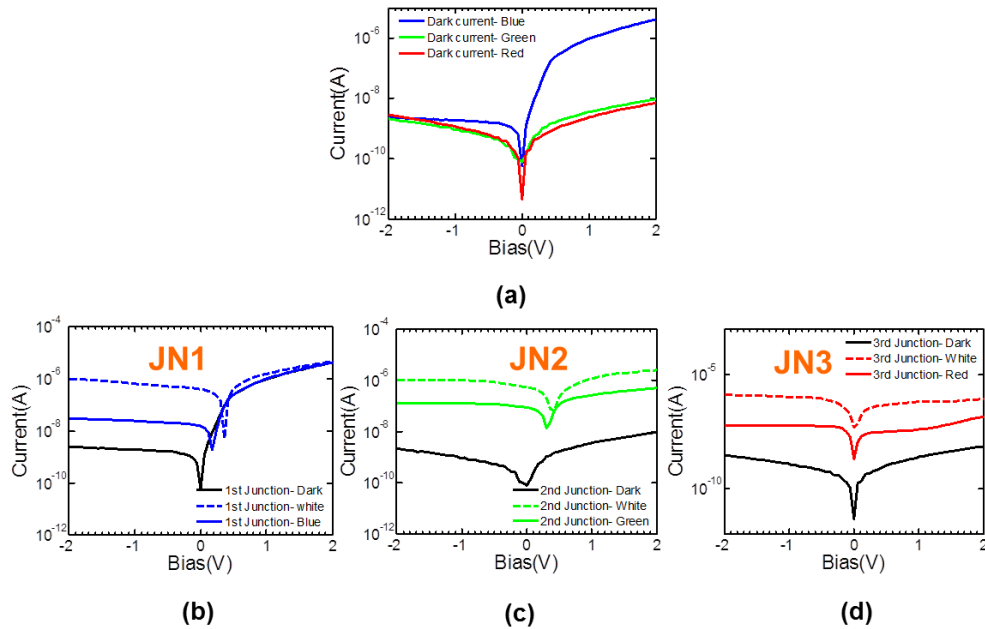
Figure 3-8 (a) Dark currents of junction 1, junction 2 and junction 3 .Comparison of junction response to junction specific color ,dark current and white light response for (b) Junction1 (b) Junction 2 and (c) Junction 3

To evaluate the performance of the device array as an imager, shadow of the symbol "+" is focused on the device array. The symbol "+" covers one column and one row of pixels, so that when the device array is illuminated with this shadow, one column and one row of pixels are under the shade of the symbol, while other pixels are illuminated without obstruction. As can be seen in figure 3-9, the shadow of the "+" can be recreated by imaging. The first and the last row of pixels are whitened out due to a disconnect in the metal interconnect for these rows, that happened during measurement. The vertical numbers represent the rows and the horizontal numbers represent the column numbers.
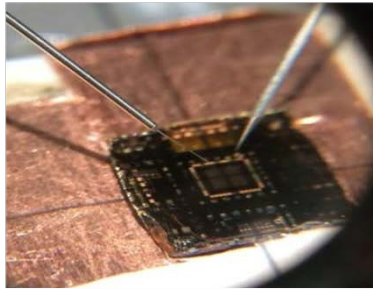
Shadow of "+" on the sample　　　　**Image of the "+" formed**
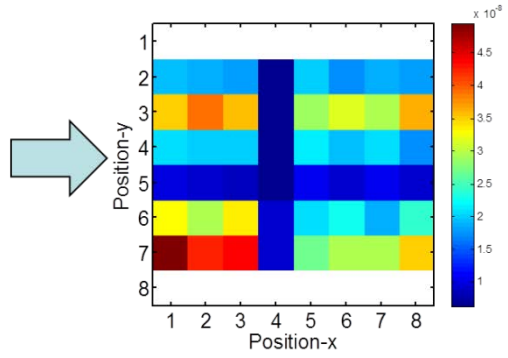
Figure 3-9 Schematic of the steps to fabricate silicon 8*8 array

3.4 Flexible Silicon PD array

3.4.1 Introduction

Flexible electronics have several alluring qualities; they are typically more rugged, lighter, portable, and less expensive to manufacture compared to their rigid substrate counterparts. The first flexible solar cell arrays were made by thinning single crystal silicon wafer cells to ~100 μm and then assembling them on a plastic substrate to provide flexibility . From the development of flexible solar cell arrays made from very thin single-crystal silicon to flexible organic light-emitting diode displays on plastic substrates, the flexible electronics industry has advanced a lot in the past several decades. Flexible can mean many qualities: bendable, conformally shaped, elastic, lightweight, non-breakable, roll-to-roll manufacturable, or large-area. Substrates used for making flexible devices must meet many optical, mechanical, electrical, magnetic, chemical and thermal properties depending on the application.

The structure of SOI used for the fabrication of flexible PD array is same as that of the one used for rigid PD array and is shown in table

Table 3-2 SOI structure of the multi-junction silicon for three color photodetection

Material	Thickness	Doping	Concentration
Si	0.2 μm	n+	1E18 cm^{-3}
Si	0.4 μm	p+	1E18 cm^{-3}
Si	1.4 μm	n+	1E18 cm^{-3}
Si	4.5 μm	p+	1E18 cm^{-3}
SiO$_2$ 1.0 μm			
Si-substrate 660 μm			

Based on the transfer printing process, we proposed and demonstrated multi-color multi-band flexible photodetector arrays based on crystalline silicon membranes and/or compound semiconductor membranes[49, 50].For this specific flexible silicon PD array application, 125 µm kapton sheet is used as the flexible substrate. The schematic of the process plan is shown in figure 3-10. The process involves removing the active silicon layer doped as n-p-n-p from the SOI substrate and transferring it to a flexible kapton sheet. Starting with a design of triple-junction Si PDs on SOI for red (R), green (G), and blue (B) color detection (Fig. 3-10(a)), the structure can be released and transfer printed onto a foreign substrates (Fig. 3-10(b)), or stacked with other semiconductor materials for multi-band detection (Fig. 3-10(c)).
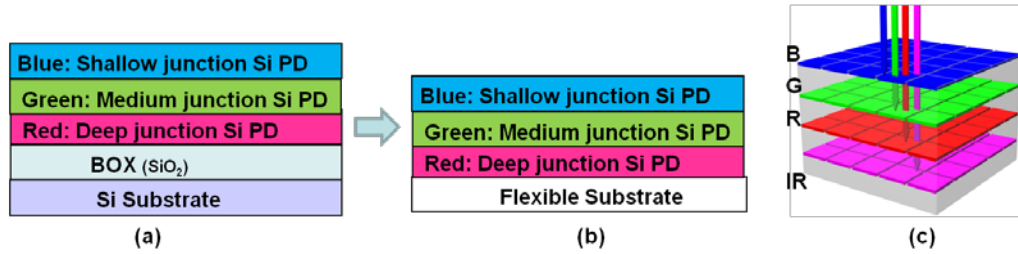
Figure 3-10 Schematics of the proposed crystalline nanomembrane based stacked multi-color multi-band photodetector arrays: (a) Triple-junction Si PDs on SOI for red (R), green (G), and blue (B) color detection. (b) Flexible RGB color PDs based on transfer printed Si-PDs on flexible substrates. (c) Multicolor multi-band PDs based on transfer printed Si/InGaAs nanomembranes.

3.4.2 Fabrication

The process flow for the device fabrication is illustrated in Fig. 3-11. SOI substrate [Fig. 3-11(a)] is first patterned with release holes, and then the top Si layer is etched to expose the underlying 1 µm thick buried oxide [BOX, Fig. 3-11(b)]. HF etching is then done to remove this oxide and release the 6.5 µm thick Si nanomembrane from

the Si handle as shown in Fig. 3-11(c). By wet transfer, this nanomembrane is transferred on to a SU-8 coated 125 µm thick Kapton sheet [Fig. 3-11(d)]. The transferred nanomembrane is 4.2 mm long, 4.3 mm wide. Regular lithography process is then performed on the Si nanomembrane transferred on Kapton. The pixel arrays were patterned and etched with reactive ion etching (RIE) process to form mesa sizes of 100 µm *100 µm [insert of Fig. 3-11(e)]; and the contact regions in each pixels were also defined by dry etching to a depth of 400nm, 2.5µm and 4.5 µm to reach the various doped layers, in order to form the three PN junctions. This is followed by metallization of the local contacts at each depth [zoom-in view insert of Fig. 3-11(g)]. Cr/Au was deposited as the contact metal by e-beam evaporation. Four interconnect layers were subsequently formed with Cr/Au in two groups (bottom interconnect pair and top interconnect pair) for the access of individual contacts of the Si-PD pixels in the PD array as shown in Fig. 3-11(h). It is worth to note here that HD4104 polyimide passivation layer was introduced for the isolation of individual interconnect lines at different depths. The HD4104 polyimide layer thickness is optimized to have a continuous interconnect layer at the edges of the mesa, where it connects to the local metal contact pad. After the deposition of the top interconnect layers by e-beam evaporation, the individual mesas/pixels can now be accessed by probing the 150 µmx150 µm interconnect metals pads at the four edges of the kapton. Shown in Fig. 3-11(i) is the final structure under bending.
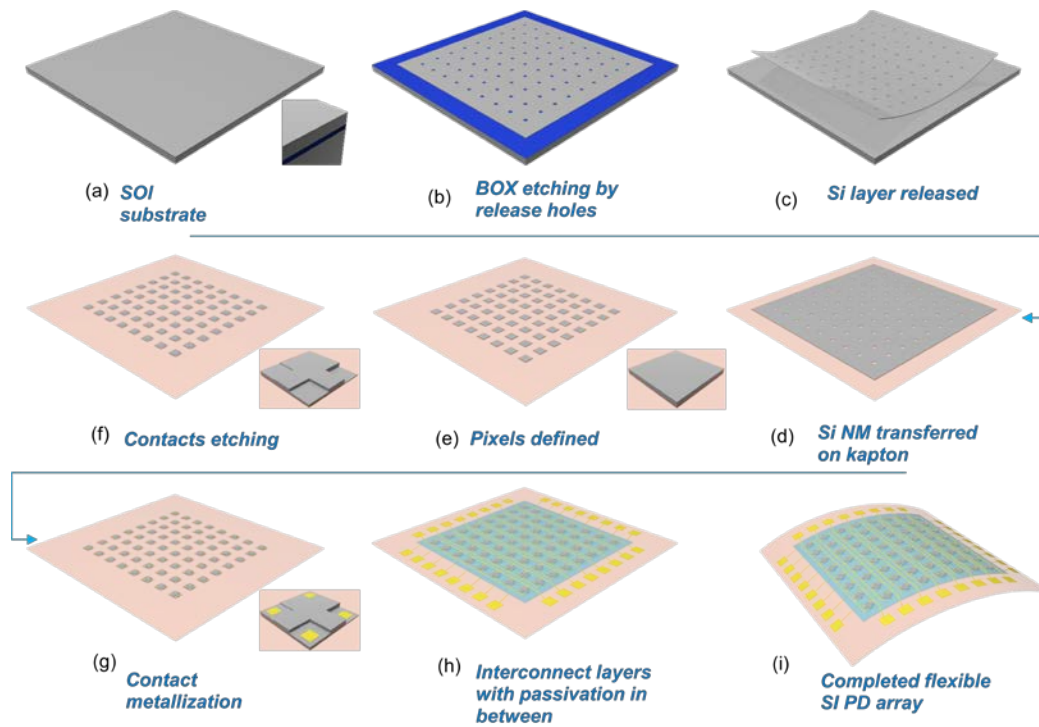
Figure 3-11 Schematic of the steps to fabricate flexible silicon 8*8 array

The process of etching the BOX layer to release the 6.5μm silicon, and transferring it to a kapton substrate is illustrated in figure 3-12 below.
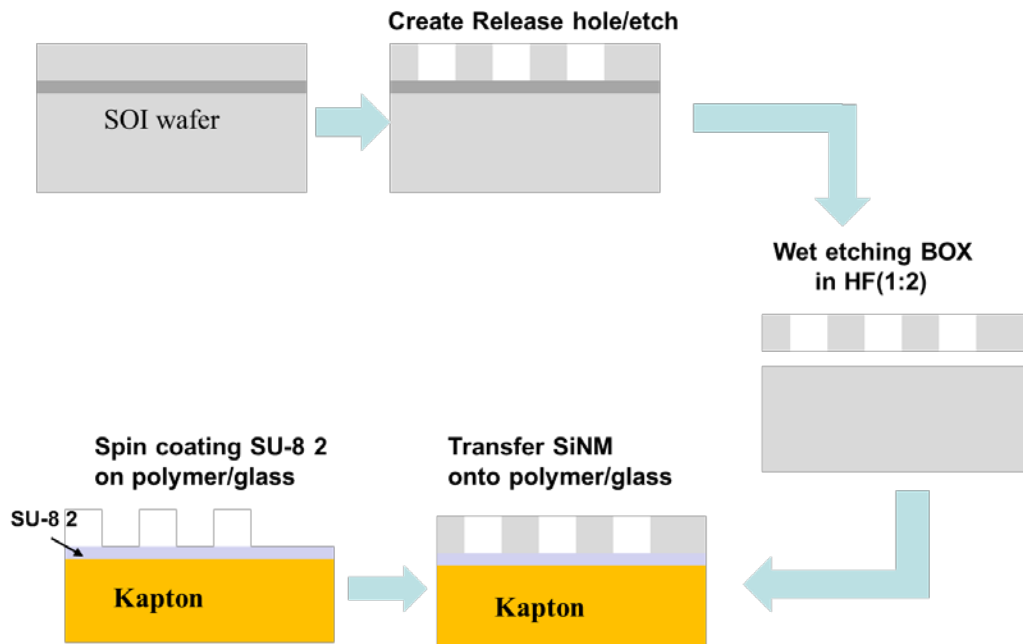
Figure 3-12 Schematic of the steps involved in releasing the active silicon layer from the SOI and transferring it to kapton

The silicon membrane is obtained by first pattering the release holes with negative resist NR9. The exposed silicon is etched in a DRIE chamber with SF_6 gas, to a depth of 6.5 μm, until the BOX layer is reached The SOI with the etched release holes is then immersed in HF, to allow for HF to enter in through the release holes and etch away the 1μm BOX layer. Once the BOX layer is etched, the top 6.5μm active Si is suspended and hangs on to the substrate by weak anchors. The SOI substrate with the suspended silicon membrane is carefully picked up by tweezers or a cleanroom wipe, and gently placed in DI water. Gentle agitation of the SOI releases the Si membrane completely from the substrate and it floats in DI water. This can be picked up gently by sides of tweezers or edges of cleanroom wipe, and placed on top of a kapton sheet, which has been coated with a thin layer of SU8-2. Hard bake of SU8 -2 is done after the transfer of

membrane, so that the Si membrane sticks firmly to the SU8. Processing of the PD array begins once the membrane has firmly adhered to the kapton.
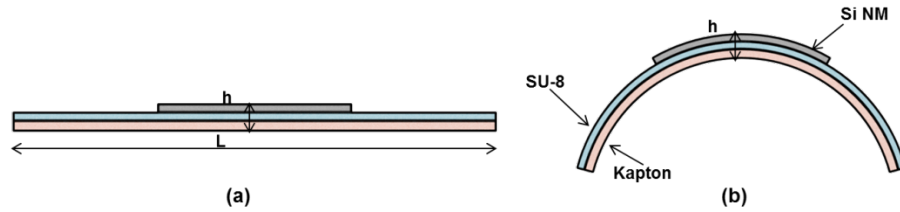
Figure 3-13 Structure of Silicon after transferring to SU8 coated Kapton sheet

Shown in Fig. 3-14 shows a crystalline Si membranes transferred on a kapton substrates by the process mentioned in figure 3- 12, before further device processing.
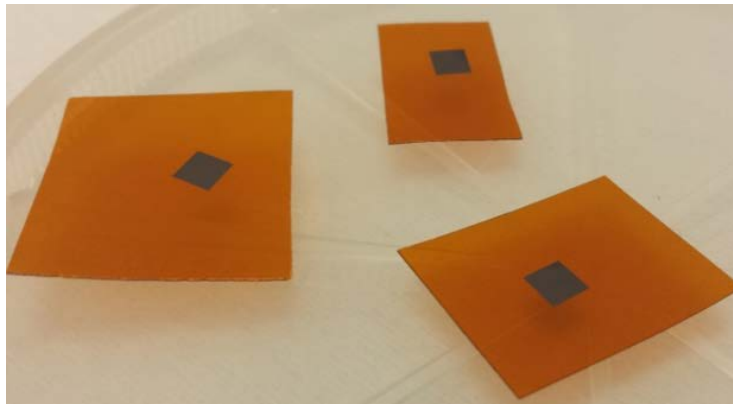
Figure 3-14 Silicon transferred to Kapton sheet

Micrographs of the devices on a kapton substrate at various stages of processing are shown in Fig. 3-15. 3-15(a) shows the definition of mesas after dry etching with SF_6 gas. The different contact regions are also defined, and the contact metal has been deposited on the four corners of the mesa to contact each of the N,P,N and P doped

layers at the surface, and at depths of 400nm, 2.5 μm and 4.5μm respectively. 3-15(b) shows the PD array after the deposition of the first polyimide layer and metallization of the bottom interconnect layers. The first polyimide layer is deposited to give the required height, so that the interconnect layer to be deposited in the next step can access the local metal pads on the mesa, without any disconnect at the mesa edges, that could arise due to too thick or too thin of a polyimide layer. The polyimide used is the photo definable HD4104. The second polyimide layer is then patterned after the bottom interconnects, and top metal interconnect layers are deposited as shown in figure 3-15(c).Again, the thickness of the passivating HD4104 layer in between the top and bottom interconnects is optimized to minimize the drop or climb of the interconnect metal at the mesa edges. A zoom in of one single pixel in the array is shown in figure 3-15(d).

(a)   (b)   (c)

(d)
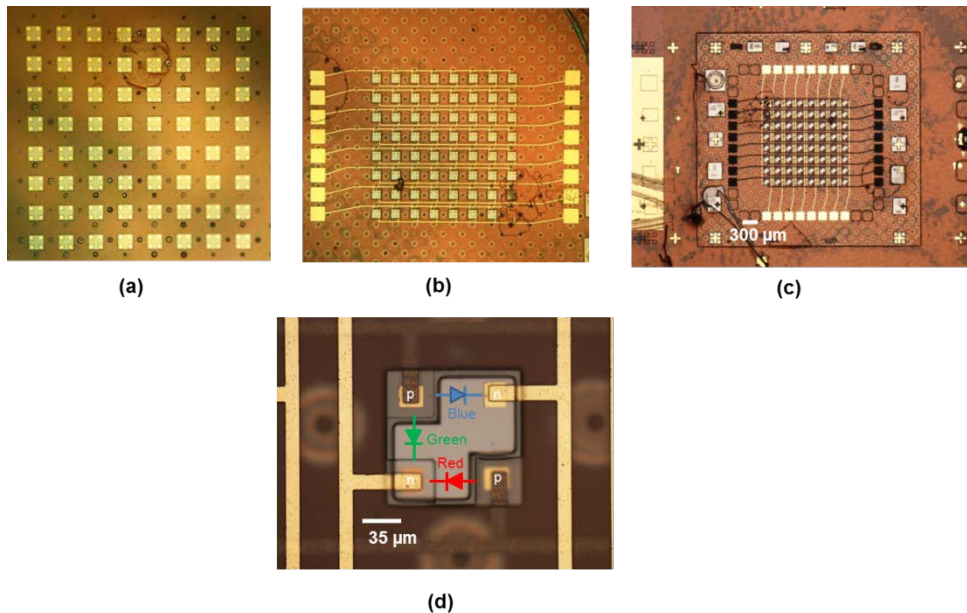
Figure 3-15 Fabrication steps (a) after pixel isolation, etching and contact metallization (b)after bottom interconnect metallization (c)after polyimide passivation and top interconnect metallization and (d) zoom in of one single pixel in the array

3.4.3 Characterization of Imager

Individual pixels were first characterized, with typical results shown in Fig. 3-16, for the first (blue), second (green), and third (red) junctions measured under 405 nm, 532 nm, and 632 nm incident wavelength respectively. All the pixels in the array were characterized, but the results of only one pixel are shown for clarity. All the devices showed uniform performance and so, the performance of the pixel shown below is representative of the performance of all the pixels. The pixel is illuminated with a light source and the response of each pixel to increasing intensities of the input light is recorded. As seen in Fig 3-16, as the intensity of the input laser is increased, the response of the photodetector also increases. Figure 3-16 (a) shows the response of junction 1 to blue laser (405nm), 3-16(b) shows the response of junction 2 to green laser (532nm) and 3-16(c) shows the response of junction 3 to red laser (632nm). I–V measurements were done at room temperature using a Keithley 2612 current source.

(a) (b) (c)
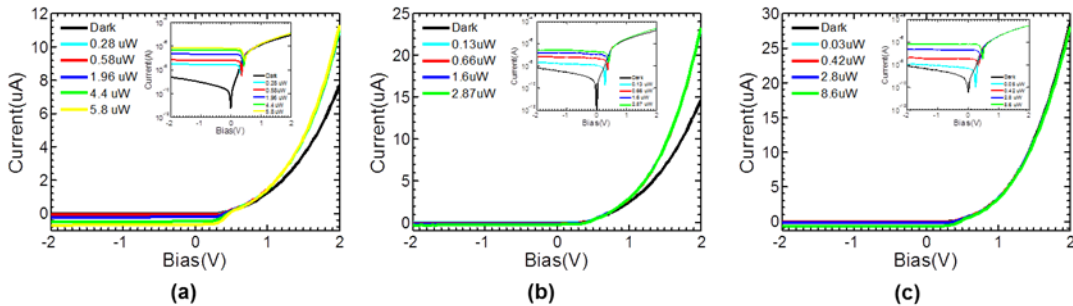
Figure 3-16 IV characteristics of the three junctions under illumination (a) Response of Junction 1 to blue laser(405 nm) (b) Response of Junction 2 to green laser(532 nm) (c) Response of Junction 3 to red laser(632 nm)

The dark current is an important factor and unit of merit in a photodetector that describes the current output from the photodetector, when biased, in the absence of a light source. A high value of dark current reduces the efficiency and detectivity of the detector, and increases noise. So, its desirable to have the dark current as low as possible. The dark currents for all junctions and devices tested show less than 10 nA over reverse bias voltage up to 2 V. For the illumination measurements, light was centered on the individual devices with a lensed fiber via a light wave probe system. Light response for each wavelength was done for various intensities and they showed a minimum of at least 2 orders of magnitude increase from the dark current.

Experiments were also performed to check the efficiency of light detection of each junction for the intended color, and hence the ability to have maximum response for the respective color, as opposed to other colors. Each junction was illuminated with all the three colors, and the response of each junction to all the three colors are recorded, as shown in figure 3-17. The intensity of blue laser used for all the three junctions is 1.96 µW, intensity of green laser used is 0.13 µW , intensity of red laser used is 2.1 µW and that of 980 nm laser is 1.8 µW.
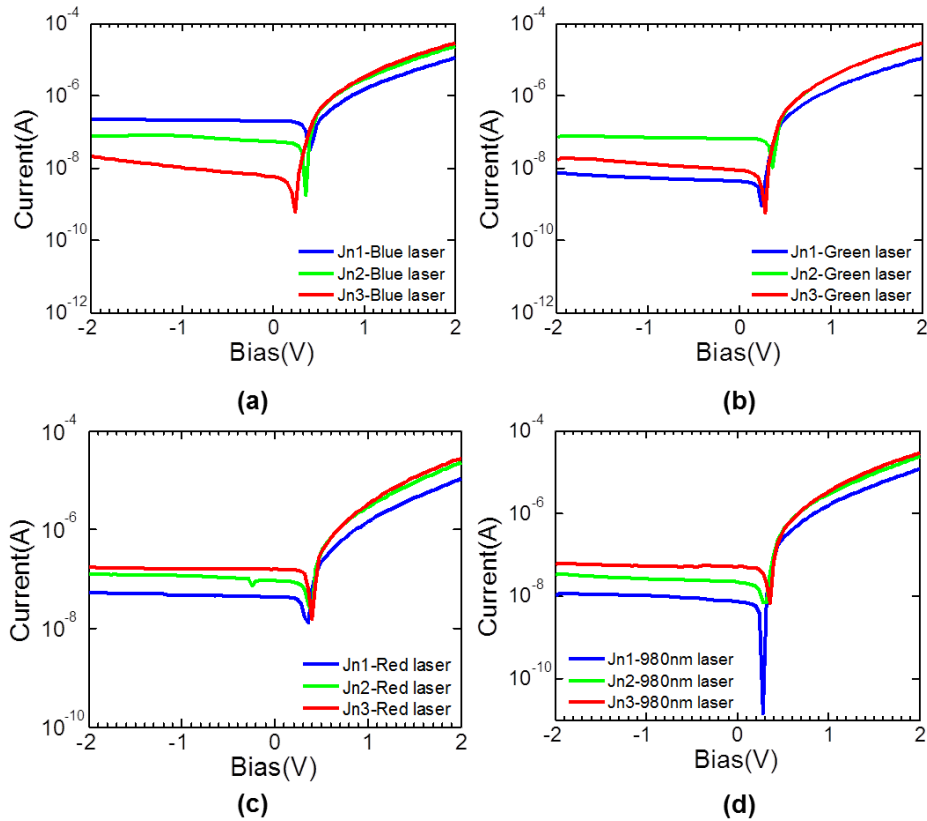
Figure 3-17 Comparison of each laser response at different junctions (a) Response of three junctions to blue laser (405 nm) (b) Response of three junctions to green laser (532 nm) (c) Response of three junctions to red laser(632 nm)

As can be seen in figure 3-17(a), when the structure is illuminated with blue laser, the maximum response is in Junction 1, as opposed to junction 2 and junction 3 , which is expected as the blue wavelength is absorbed mostly on the surface. Similarly, for green laser, maximum response is in junction 2 and for red laser, maximum response is in junction 3. For 980nm laser, the maximum response is found to be in junction 3 as well, which is the deepest junction.

The measured responsivities for blue, green and red wavelengths are 0.1 A/W, 0.09 A/W, and 0.07 A/W, respectively. Additionally, each junction was also tested with two other wavelengths, to calibrate the color selective responsivities. All the results are

42

shown in Fig.3-18(a), with different symbols. Note excellent agreements were obtained for both blue (PN-J1) and green (PN-J2) junctions. Some discrepancies were found between measured and simulated responsivities for red (PN-J3) junction, which may be related to the differences in the actual power being absorbed for this junction. This might also be due to the etch depth for the red junction not being deep enough to gather all carriers.
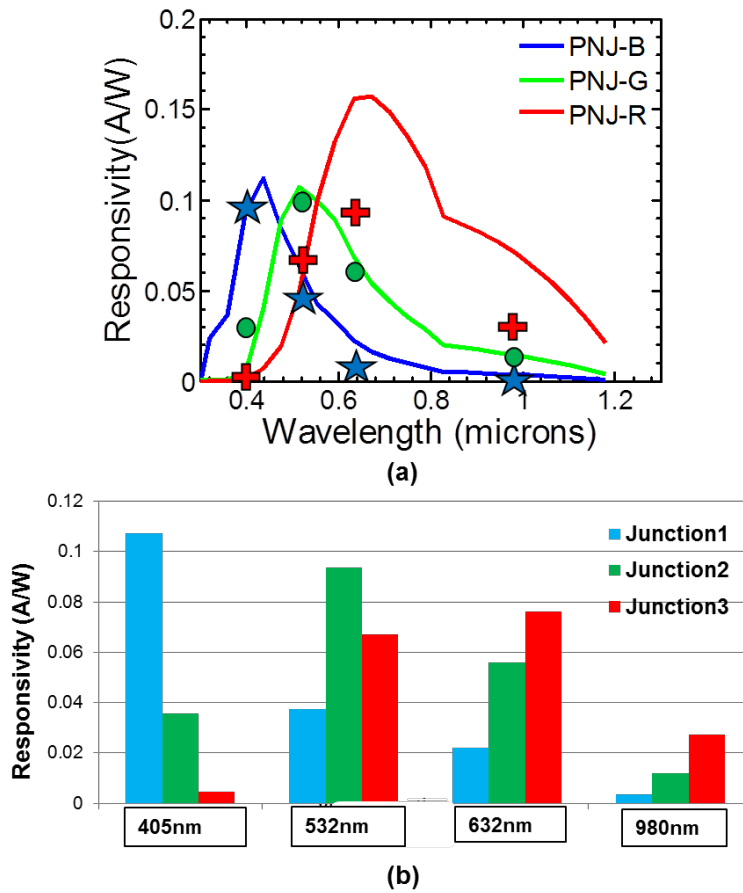
Figure 3-18 (a) Simulated (line) and measured (symbol) responsivities for the triple-junction RGB detector arrays. Tests were done with lasers at wavelengths of 405 nm, 532 nm, 630 nm, and 980 nm (b) Responsivities of the three junctions for all wavelengths showing the maximum responsivity for each junction is for the respective color.

Array performance was also evaluated by measuring uniformity of pixel devices and the imaging capabilities. By measuring the spectral responsivities for each junction, color (spectral) information can be resolved based on post-imaging data process, which can be used to construct color images. Imaging was done using a QTH white light source that was focused on the 8 x 8 silicon photodetector array through a chrome mask with the letter "H". On the array, the pixels that are not covered by the area of the letter "H" is illuminated by the light source and the area covered by the letter "H" is in dark. The resulting image formed after data handling is shown in Fig. 3-19. The horizontal and vertical numbers in the figure correspond to the row and column number of the array. The two horizontal blue rows in Fig. 3-8(a) and 3-8 (b) occur due to lower responses in rows 1 and 2, as opposed to the others. Each square in the figures represent the difference in the measured response current and dark current for that specific pixel/device. The scale bar on the right side of each figure, shows the range of values in the square. Non-uniformity in this difference is depicted as difference in the color of pixels in the "non-H" region. Imaging quality can be improved by increasing the pixel size and improving the uniformity of the imager arrays. It is also worth noting that the illumination white light source used in our measurements is not ideally a collimated beam, which creates unnecessary shadow effect when the "H" chrome shadow mask is used for the imaging demonstration.

(a)   (b)   (c)
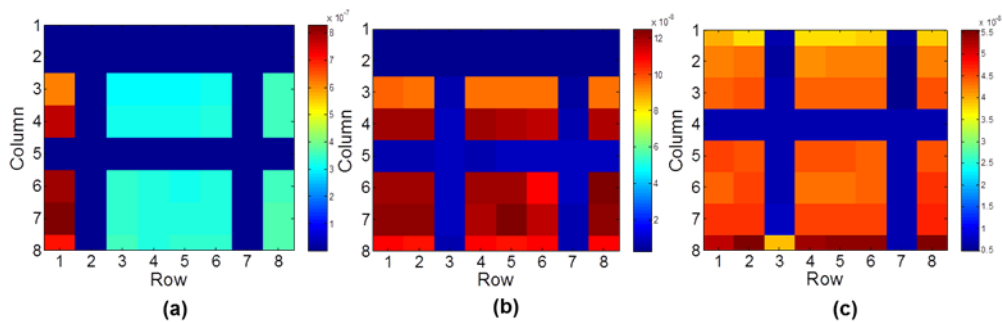
Figure 3-19 Images of the letter "H" reproduced by biasing the (a) Blue (b) Green and (c) Red junction of all the 64 devices in the array

To demonstrate the flexibility of the photodetector array, bending tests were also performed. The kapton sheet housing the array was placed inside a lens/filter holder (with bending radius of 8 mm [51])and the screws of the apparatus was adjusted to bend the kapton and hence the photodetector array. I–V measurements were taken while the device was in the bent state. It is to be noted that 8mm is just the maximum bending radius the kapton was bent for our bending tests, but that is not the limit it can be bent to. A comparison of the dark currents before and during the bending shows that the device performance is maintained during the bending, and there is no noticeable degradation in dark current. This can be seen in figure 3-20.

(a) (b) (c) (d)
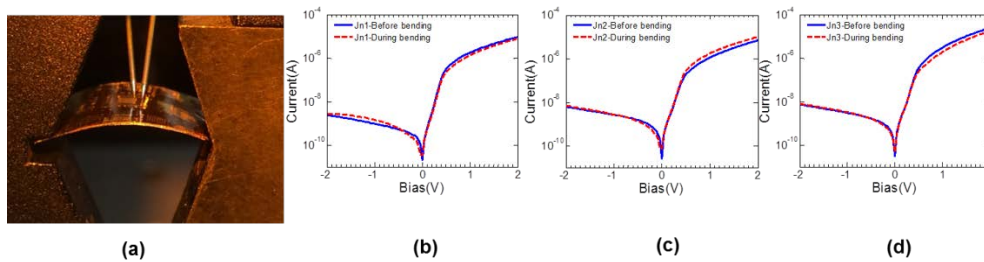
Figure 3-20 Comparison of dark currents of three junctions before and during bending (a) Flexible Si PD array in bent state (b) Response of Junction1 (c) Response of Junction2 (d) Response of Junction3

The flexible Si PD array is also illuminated with white light, while in the bent state and the response of the first, second and third junctions is measured. Figure 3-21 illustrates the comparison between the responses of the three junctions before bending and during bending, for all the three junctions for a single pixel. As can be seen, the photoresponse does not degrade even in the bent state, and is indistinguishable from the photoresponse before bending.

45
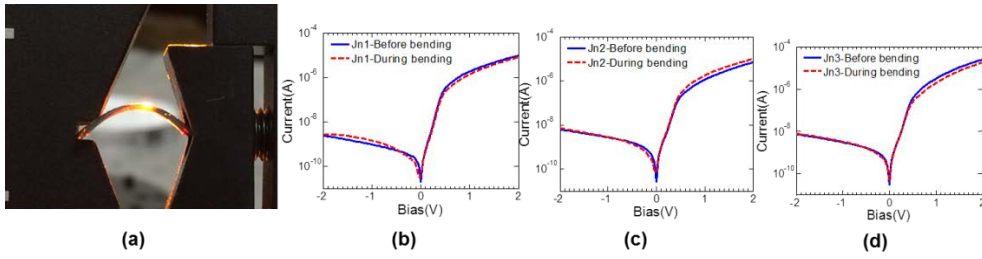
Figure 3-21 Comparison of response of three junctions to illumination before and during bending (a) Flexible Si PD array in bent state (b) Response of Junction1 (c) Response of Junction2 (d) Response of Junction3

Chapter 4

Integrated photodetectors

4.1 Background

Multi-band and multispectral imaging has various applications in remote sensing, automotives, industrial surveillance systems and medical field. Simultaneous acquisition of visible and infrared (IR) is especially of interest, according to the recent market trends. Several approaches have been reported in literature to capture and separate visible and NIR information of a scene. The main methods used currently to sense and separate visible and IR wavelengths involve 1) use of color filter arrays(CFAs) 2)use of external mechanical filters 3)use of depth dependent absorption property of materials. Most of the approaches to detect visible and IR wavelengths fall under the first category, where a GRGB pattern of color filters is placed over the imager sensors to detect colors. The GRGB is replaced with a RGBW, where W stands for panchromatic, which is sensitive to all wavelengths[52]. Due to the large sensitivity of W pixel to visible wavelengths and the large sensitivity of the RGB cells to NIR wavelengths, this approach has issues. Some attempts have been made to rectify the errors, by using photonic crystals with defect layers to form IR blocking layers at each RGB pixel location, leaving W pixel unfiltered. In the second category, the two main approaches are either to capture the same scene through two separate cameras simultaneously or to use an IR blocking filter or a visible blocking filter to simultaneously take two images of the same scene. Both of these methods require lot of post processing like image fusion[53, 54], and the need to mechanically replace filters or use two cameras, which make them expensive, bulky and slow. Also, more processing power is needed to analyze and compare two separate images. Lyu et al [55] have made a vertically integrated

47

photodiode structure (VIPS) which utilizes the method in the third category. Here, a deep buried photodiode was formed beneath the normal RGB photodiodes, to absorb and detect the NIR wavelength, while the color filters on top for R,G,B selection , detect visible radiation, similar to a CFA. Since the area of the deep photodiode and the R,G,B pixels are different, the resolution of IR images will be quarter of that of visible images. Langfelder [56] proposed a topology to detect visible and IR radiation, based on the principle of Transverse Field detector, which also relies on the absorption properties of radiation in silicon. Here, by suitable biasing of the collecting junctions on the surface, the charge carriers generated at different depths can be collected by means of transverse electric fields. Martin et al [11] reported a Visible InGaAs FPA, where they have increased the quantum efficiency of InGaAs in the visible band, by removing or thinning the InP substrate, which absorbs most of the visible light in a back illuminated structure.

The method used in this paper falls into the third category. In semiconductor materials, the absorption depth of photons varies with the energy of photons. This property can be utilized to build a multicolor detector, using silicon, by having several PN junctions stacked on top of each other, as the absorption depth of Si varies over several orders of magnitude over the visible range. By building a vertically integrated structure, we can avoid the inevitable transmission loss, color aliasing effect and resolution limitation encountered with color filter array (CFA) based sensor arrays[42]. Thus, the carriers generated at various depths due to the difference in penetration depth of the different components of visible light can be used to determine the wavelength of the incident light. Since the bandgap of silicon limits the detection of wavelengths beyond 1.1 μm, we need a different material, like InGaAs with band gap of 0.75eV, capable of detecting wavelengths up to 1.68μm, to detect NIR radiation.

Heterogeneous integration of dissimilar classes of semiconductor materials into a single 2D or 3D system is beneficial for many existing and emerging applications like infrared imaging cameras, addressable sensor arrays , hybrid Si CMOS circuits, nanowire devices and multifunctional RF communication devices. Epitaxial growth [57-61] and wafer level bonding([62-66]) are two widely used methods to achieve such kind of integrated systems(A). Both these processes have some important drawbacks. Wafer bonding can be direct wafer bonding(with or without SiO_2)[67-70] or adhesive bonding, with the help of an intermediate layer[63, 71, 72].Although the bonding process works well in several cases, it suffers from issues like 1) Inability to scale to large areas 2) inability to scale to more than few layers in the third dimension. 3) Incompatibility for use with structured or low temperature materials/substrates.4) challenging fabrication and alignment for the through wafer electrical interconnects 5) demanding requirements for bonding planar surfaces 5) bowing and cracking occurring from mechanical strains due to difference in thermal expansion of dissimilar materials. Epitaxial growth uses molecular beam epitaxy or other such means to grow thin layers of semiconductor materials directly on the surface of wafers and other materials. This method overcomes many issues of the wafer bonding process, but due to the requirements of epitaxial growth, there are severe restrictions on the quality and type of materials that can be grown [73]. To overcome the shortcomings of both these methods, transfer printing process has been developed and widely used to integrate, stack and create heterogeneously integrated devices[49, 74]. In most cases, a polydimethylsiloxane (PDMS) stamp is mostly used as the intermediate medium to transfer the membrane layer from the parent substrate to the new substrate. The process of PDMS transfer is summarized in the figure 4-1. The process consists of picking the membrane from the donor wafer with PDMS stamp, at high velocity, and then printing the membrane on the new substrate, and peeling off the PDMS at a low velocity.

This process transfers the membrane or devices from donor substrate to a new substrate.
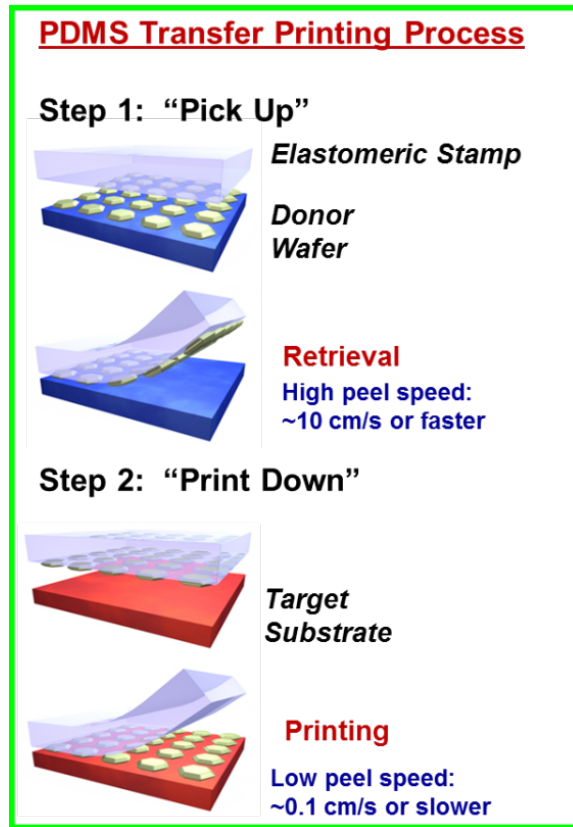
Figure 4-1 PDMS transfer printing steps [49]

Here, a heterogeneously integrated silicon and InGaAs photodetector array, which is capable of detecting both visible and IR light, by the process of PDMS transfer printing process, is presented. The silicon detector has a vertical n-p-n-p structure, capable of detecting blue, green and red colors of the visible spectrum by utilizing the wavelength dependent absorption property of silicon, while the InGaAs detector has a PIN structure with a 2 μm intrinsic (I) region, which can detect the NIR wavelengths. The principle and working of the silicon detector has already been discussed and

demonstrated in an earlier paper[75]. Based on transfer printing process, these crystalline silicon membranes based photodetector arrays are transferred onto InGaAs substrate, enabling heterogeneously integrated photodetector arrays for focal plane array imaging and sensing applications. Using this filterless approach, a single pixel is sensitive to visible and IR wavelengths, without the use of mosaics or the need for interpolation. This approach also has the advantage of capturing visible and IR radiation in a single shot, with the same resolution, while avoiding the complicated process steps needed to deposit IR blocking filters at pixel level. Such a heterogeneous structure can be useful in various areas like bio photonics, security monitors, automotive cameras, fluorescent imaging, spectrometer on a chip, LADAR, free space optical communications.

4.2 Vertically integrated Si/InGaAs Imager

4.2.1 Introduction

The first layout of integrated photodetectors that was explored is the vertically integrated structure, where Si from SOI is vertically stacked on top of InGaAs PIN layers on InP substrate. The structure of the SOI and InGaAs used for fabrication is shown below, in Table 4-1.

Table 4-1 (a) SOI structure (b) InGaAs PIN structure

Material	Thickness	Doping	Concentration
Si	2um	N Diffused till 1um	1e17
SiO2 500nm			
Si-substrate 660 µm			

(a)

Layer	comment	Material	x	y	Thickness (Å)	Dopant	Level (/cm³)	Type
9		In(x)Ga(1-x)As	.53	-	500	Be	mid E19	p
8		InP			2,000	Be	mid E18	p
7		In(x)Al(y)Ga(1-x-y)As	.53	0.0-0.226	400	UID	-	-
6		In(x)Ga(1-x)As	.53	-	20,000	UID	<1e15	-
5		In(x)Al(y)Ga(1-x-y)As	.53	0.226-0.0	400	Si	mid E16	n
4		InP			200	Si	low E18	n
3		In(x)Ga(1-x)As	.53	-	500	Si	mid E18	n
2		InP			3,000	Si	mid E18	n
1		In(x)Ga(1-x)As	.53	-	200	Si	mid E18	n
	Substrate							

(b)

4.2.2 Fabrication
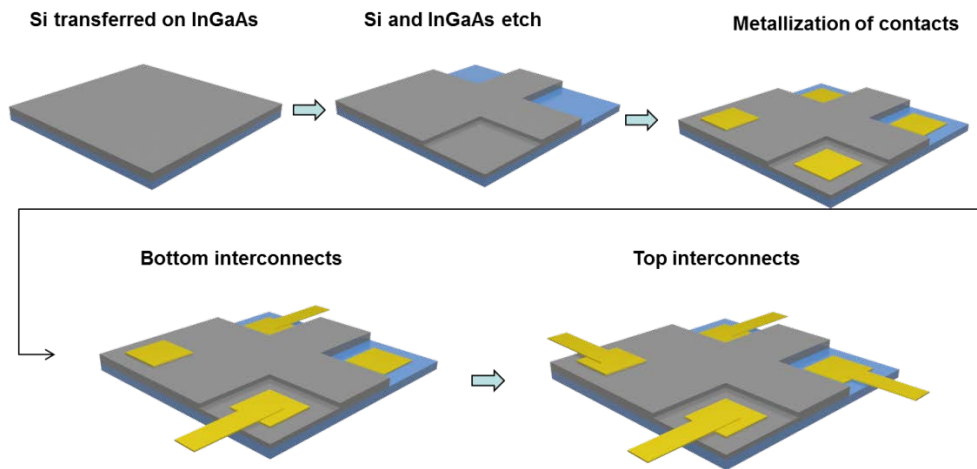
Figure 4-2 Fabrication steps involved in making vertically integrated Si and InGaAs Imager

Figure 4-2 shows the steps involved in the fabrication of a vertically integrated Si /InGaAs 8x8 photodetector array. The fabrication process begins with transferring the Si

membrane on top of the InGaAs substrate. This is done by the PDMS transfer printing process. The SOI wafer with 2µm active Si layer is initially immersed in HF to etch the SiO_2 layer. This leaves behind the Si active layer, which is anchored to the Si substrate at the four corners. Placing the PDMS on top of the active Si layer and applying pressure, breaks the anchors and attached the Si layer to the PDMS due to van der waals forces. By quickly retrieving the PDMS at high velocity, the 2 µm active layer can be picked up by the PDMS. This PDMS is then placed on top of the new substrate, InGaAs, and peeled off at low speed. This leaves behind the active Si layer on the surface of InGaAs. Mesas are defined by dry etching Si first and then InGaAs to isolate the pixels from each other. Si and InGaAs are then etched to their n and p regions, by first defining the 20µm etch area by photolithography and then dry etching by DRIE .Once the n and p regions are defined for the Si and InGaAs , local contacts are made by deposition using an e-beam evaporator. This is followed by metallization of the bottom pair of interconnects , to enable probing the p and n contacts without damaging the mesas. HD4104 polyimide is then deposited to act as a passivation layer to separate the bottom interconnect metal from the top interconnect metal. The passivation layer is followed by deposition of the top and final interconnect metal using the e-beam evaporator. The pixels are 100µmx100µm and separated by 100µm. Fig 4-3 shows the optical and SEM images of a single pixel and the 8x8 array of the completed vertically integrated heterogeneous structure.
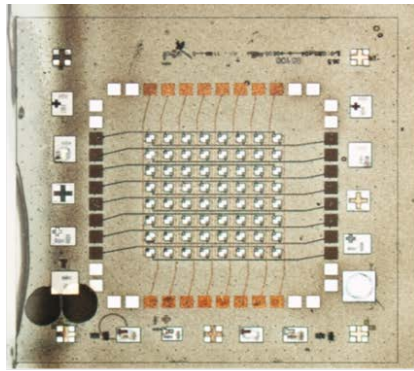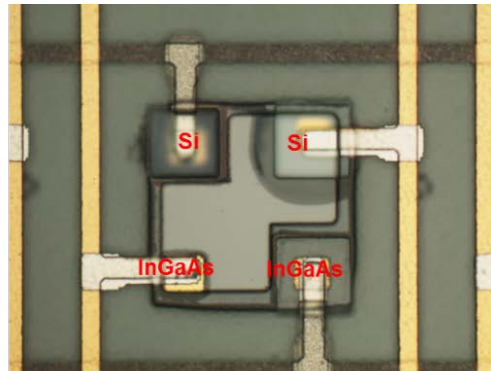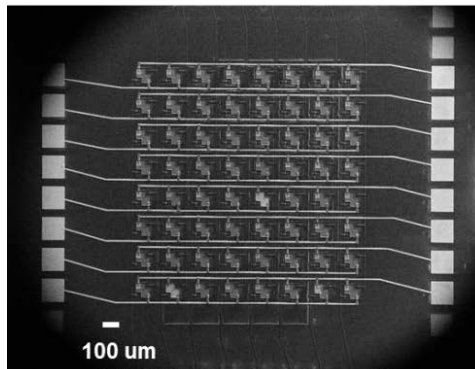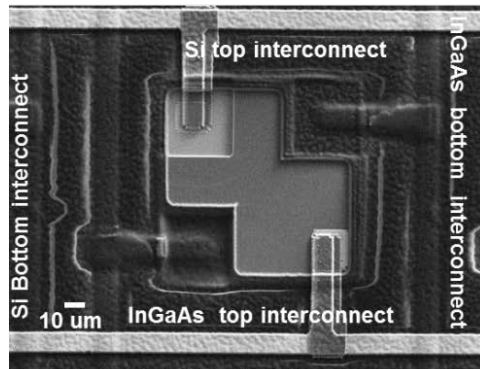
Figure 4-3 Images of completed vertically integrated imager. Optical images of (a) Complete 8*8 Si/InGaAs vertically integrated array (b) Single pixel and SEM images of (c) the completed array and (d) single pixel.

4.2.3 Characterization
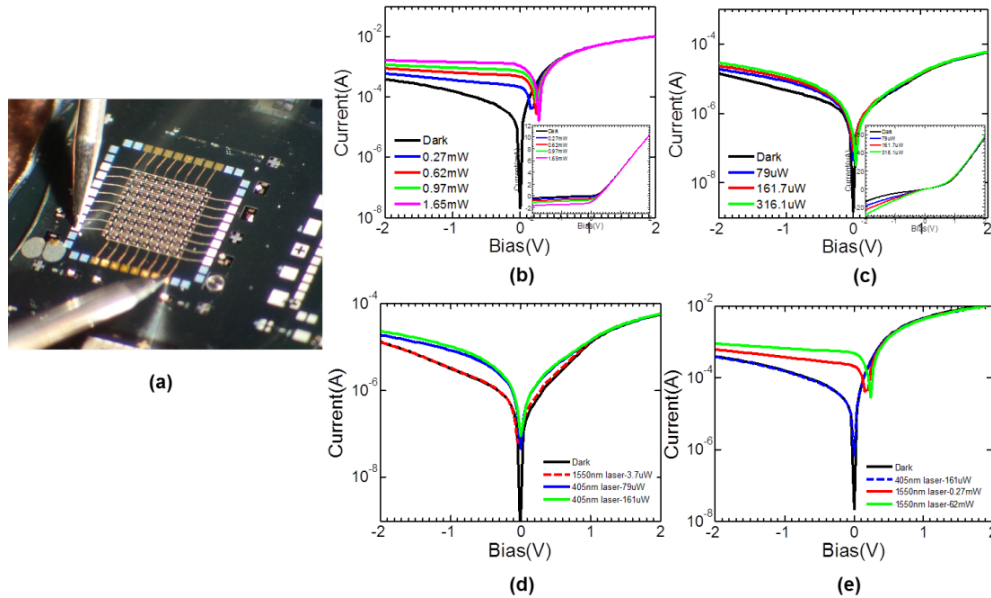
Figure 4-4 IV characterization of the vertically integrated imager. (a) Completed imager array (b) Response of InGaAs PD to 1550 nm laser (b) Response of Si PD to 405nm laser (c) Response comparison of Si junction to 1550nm and 405nm laser (d) Response comparison of InGaAs junction to 1550nm and 405nm laser

IV characteristics of the Si and InGaAs photodetector are separately analyzed and compared, as shown in Fig 4-4. Fig 4-4(b) shows the response of Si PD to increasing intensities of blue laser(405nm wavelength). Fig 4-4 (c) shows the response of InGaAs PD to increasing intensities of 1550nm wavelength. For both the junctions, it is observed that as the incident intensity increases, the photoresponse of the respective junction increases. Fig 4-4 (d) and (e) shows the comparison of the responses of the two junctions for incident wavelengths in visible and IR range. Fig 4-4 (d) shows the response of the Si PD to both 405nm wavelength and 1550 nm wavelength. As is expected, there is no response to 1550nm wavelength incident light, but response increases when the incident wavelength is in visible range. Similarly, it can be observed in fig 4-4(e) that there is no photoresponse in InGaAs for visible light, but photoresponse increases once

the incident wavelength is 1550nm. This proves that the Si junction and the InGaAs junction are responsive to only the visible and IR wavelengths respectively, and are mutually exclusive.

4.3 Adjacent Si/InGaAs imager

4.3.1 Introduction

While the vertical stacking offers the best possible spatial resolution, the fabrication process is much more involved due to the challenges in patterning of very thick pixels (~9 μm deep) and additional layers of planarization and passivation of polyimides for the formation of additional inter- connect layers. Here, we present the fabrication process and measurement results of another layout, the lateral/adjacent configuration, which can have slightly reduced complications in device processes for higher yield process-critical towards larger pixel arrays, at a cost of reduced spatial resolution. Based on the PDMS transfer printing process [49, 73, 76-78], we proposed and demonstrated flexible multi-color multi-band photodetector array based on crystalline silicon membranes and/or compound semiconductor membranes. Shown in Fig. 4-5 are the schematics of the proposed heterogeneously integrated multi-color multi-band photodetector array. Starting with a design of triple-junction Si PDs on SOI for red (R), green (G), and blue (B) color detection (Fig. 4-5(a)), the structure can be released and transfer printed onto an InGaAs substrate (Fig. 4-5(b)), or stacked with other semiconductor materials for multi-band detection. One pixel, comprising of one silicon and one InGaAs photodetector is shown in Fig. 4-5(c). The principle and process reported here can also be applied to a wide range of material systems, for multi-color multi-band imaging systems and spectrally resolved sensing systems for various applications. Thickness of each layer of the silicon structure was optimized based on the

penetration depth of blue, green and red wavelengths, and the design simulation was done using Medici   software. Similarly, InGaAs PIN structure   on InP substrate   was designed for NIR detection. The optimized structure for Si and InGaAs is shown in Table 4-2. Simulated responsivities for the silicon triple junction design and the InGaAs single junction design is shown in Figure 4-6.

Table 4.2 Structure of (a) Silicon and (b) InGaAs used in simulation and fabrication

Material	Thickness	Doping	Concentration
Si	0.2 μm	n+	$1E18\,cm^{-3}$
Si	0.4 μm	p+	$1E18\,cm^{-3}$
Si	1.4 μm	n+	$1E18\,cm^{-3}$
Si	4.5 μm	p+	$1E18\,cm^{-3}$
SiO$_2$ 1.0 μm			
Si-substrate 660 μm			

(a)

Material	Thickness	Doping	Concentration
$In_{0.53}Ga_{0.47}As$	80 nm	p	$Mid\,E19\,cm^{-3}$
$In_{0.53}Ga_{0.47}As$	2000 nm	i	$Low\,E14\,cm^{-3}$
$In_{0.53}Ga_{0.47}As$	400 nm	n	$Low\,E19\,cm^{-3}$
InP	150 nm		UNDOPED
$In_{0.53}Ga_{0.47}As$	150 nm		UNDOPED
InP substrate			

(b)
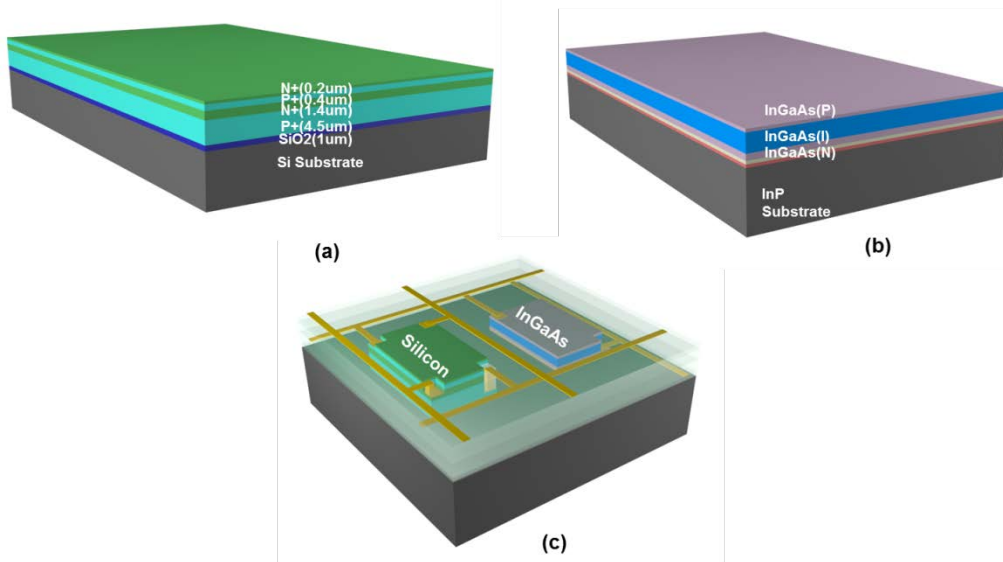
Figure 4-5 Schematic of the proposed device (a) structure of SOI (b) structure of InGaAs and (c) structure of the proposed heterogeneous structure
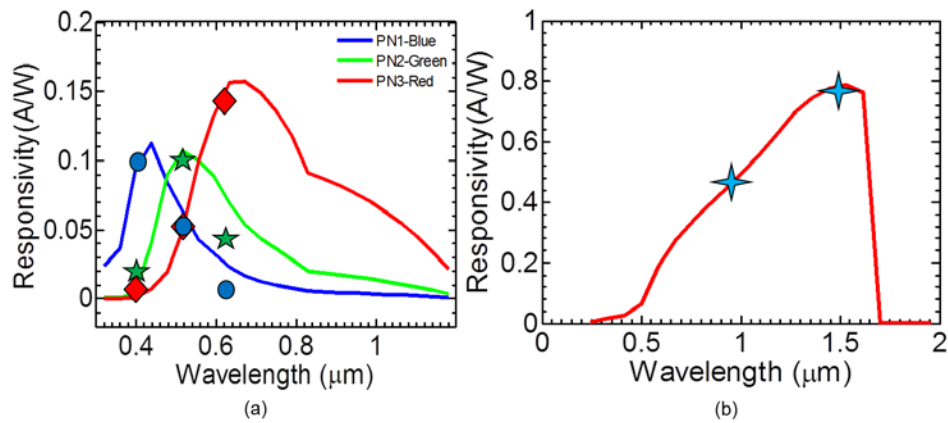
Figure 4-6 Simulated(solid lines) and measured(symbols) responsivity for a) silicon (R,G,B) and b) InGaAs (IR – 980, 1550nm)

4.3.2 Fabrication

Going further with our previous transfer printing work on flexible silicon 3 color array[75], which was based on membrane transfer, due to the addition of InGaAs for NIR detection in this paper, the fabrication process requires a different approach. Since the design utilizes a side by side/adjacent layout, we employed a transfer printing technique by which we can pick up the completed individual silicon mesas from the SOI substrate and transfer them adjacent to the InGaAs mesas by precise alignment. The process begins with fabricating the silicon mesas on rigid substrate by dry etching. Each corner of the mesa is used for depositing local contact pads, after etching them to the required depths for blue, green and red detection. This is followed by release-hole pattern and etching, to define holes in Si. These 6 μm diameter release holes are etched in the silicon mesa in order for HF to reach the underlying SiO_2 and etch it. HF etching was done for a short duration first to under etch the buried oxide under the silicon mesa. This is followed by a resist coating and photolithography process, which leaves behind photoresist only in the previously under etched areas. The SOI substrate is then immersed in HF to completely etch away the SiO_2 underneath the silicon mesas through the release holes. This separates the 6.5 μm active Si layer from the silicon handle (substrate). After this step, the only support for the silicon mesas is the photoresist pedestals. A PDMS stamp is used to pick up these loosely held Si mesas. Simultaneously, the InGaAs substrate is processed by defining the mesas, etching the contacts and metal deposition to form the p and n contacts. A thin layer of SU-8 is spun on the InGaAs substrate to increase the adhesion of the Si mesas to the InGaAs substrate. Once the InGaAs is ready to receive the silicon mesas, the PDMS stamp is precisely aligned so that the silicon mesas on the PDMS can be placed adjacent to the InGaAs mesas. Once the silicon mesas are transferred to InGaAs, PDMS stamp is removed, leaving behind the Si mesas on InP

59

substrate, aligned adjacent to the InGaAs mesas. Four interconnect layers were subsequently formed with Cr/Au for the access of individual contacts of the Si-PD pixels in the PD array. HD4104 polyimide was used as the passivation layer for the isolation of individual interconnect lines of Si and InGaAs at different depths. All the detectors have length of 100 μm and width of 200 μm, with the silicon PDs having height of 6.5 μm and InGaAs PD with 2.56 μm. The process flow schematic is outlines in figure 4-7.
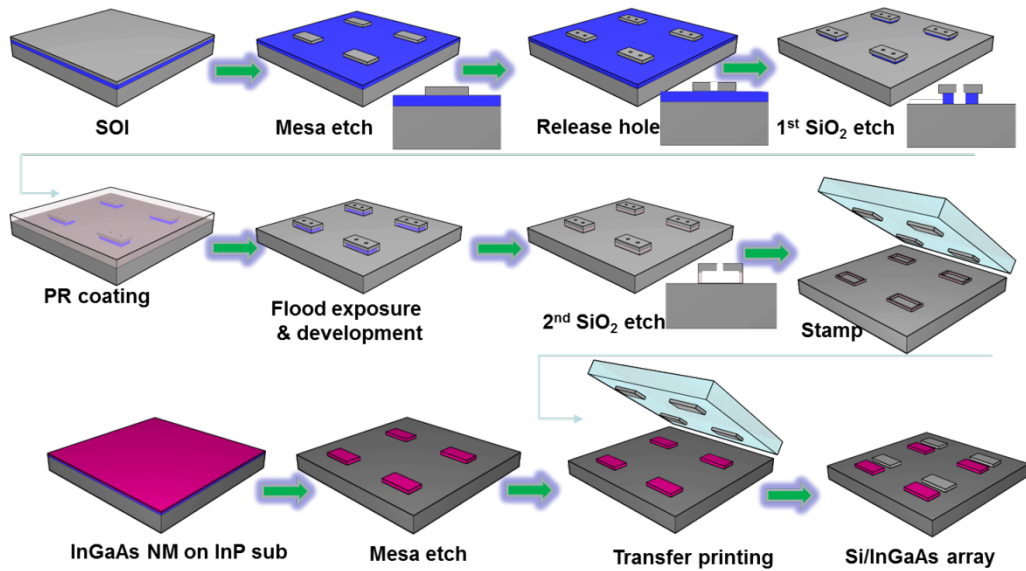
Figure 4-7 Process flow for the fabrication of adjacently placed heterogeneously integrated Si and InGaAs photodetectors.

Micrographs of the fabricated device are shown in Fig 4-8(a) shows one pixel, which comprises of one silicon and one InGaAs photodetector. Shown in 4-8(b) is a micrograph of the 4x4 array of the heterogeneous detectors, with interconnect pads on each of the four sides. The array consists of 16 Si photodetectors and 16 InGaAs

photodetectors placed adjacent to each other. Figure 4-9 shows the SEM of one pixel, comprising of one silicon and one InGaAs photodetector.

(a)   (b)
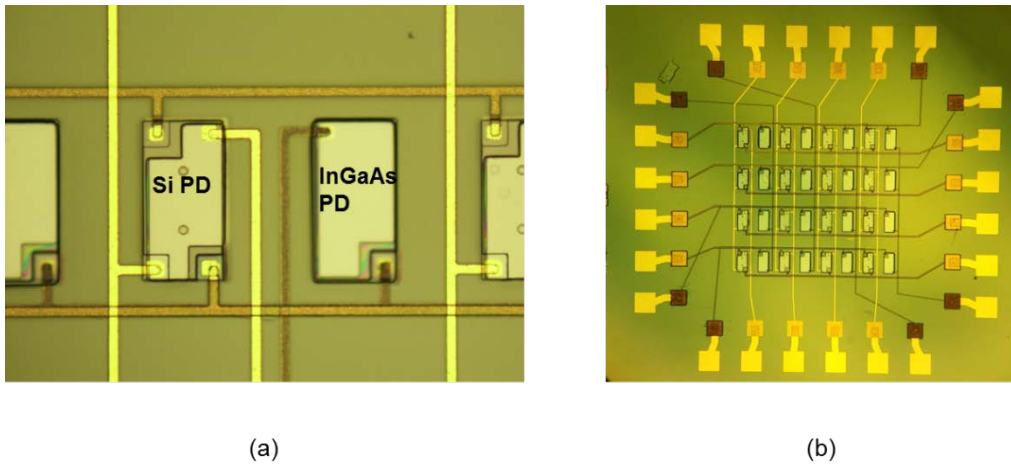
Figure 4-8 Micrographs of a) One pixel and b) 4x4 array of Si/InGaAs PDs
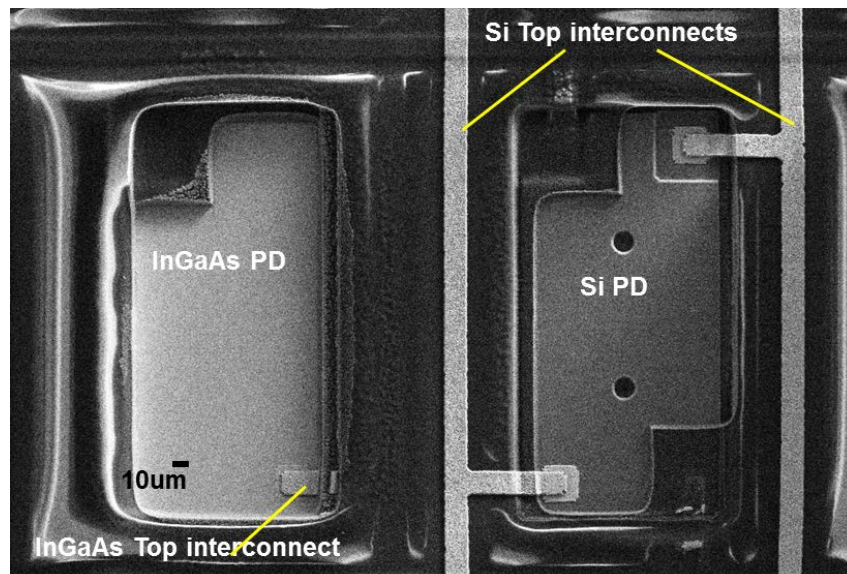
Figure 4-9 SEM image of a single pixel comprising of a Si photodetector and an InGaAs photodetector

4.3.3 Characterization- IV tests

Individual pixels of Si and InGaAs were first characterized, with typical results shown in Fig. 4-10, for the first (blue), second (green), and third (red) junctions measured under 405 nm, 532 nm, and 632 nm incident wavelengths respectively, for silicon PD and under 980 nm and 1550 nm incident wavelengths for InGaAs PD. IV measurements were done at room temperature using a Keithley 2612 current source. The dark currents for all junctions and devices tested show less than 20 nA over reverse bias voltage up to -2 V. For the illumination measurements, light was centered on the individual devices with a lensed fiber through a light wave probe system. Response of the silicon and InGaAs detectors were measured for different input light intensities and they showed a notable increase from the dark current. The measured responsivities in silicon PD for the blue, green and red wavelengths are 0.09 A/W, 0.1 A/W, and 0.15 A/W, respectively and the measured responsivities in InGaAs PD for the 980 nm and 1550 nm wavelengths are 0.5 A/W and 0.8 A/W. All the results are shown in figure 4-6, with different symbols for the various junctions. Reasonable agreement was found between the measured values of responsivity and that predicted by simulation for the silicon photodetectors. The InGaAs photodetectors had excellent agreement between the simulated and measured values of photo response.
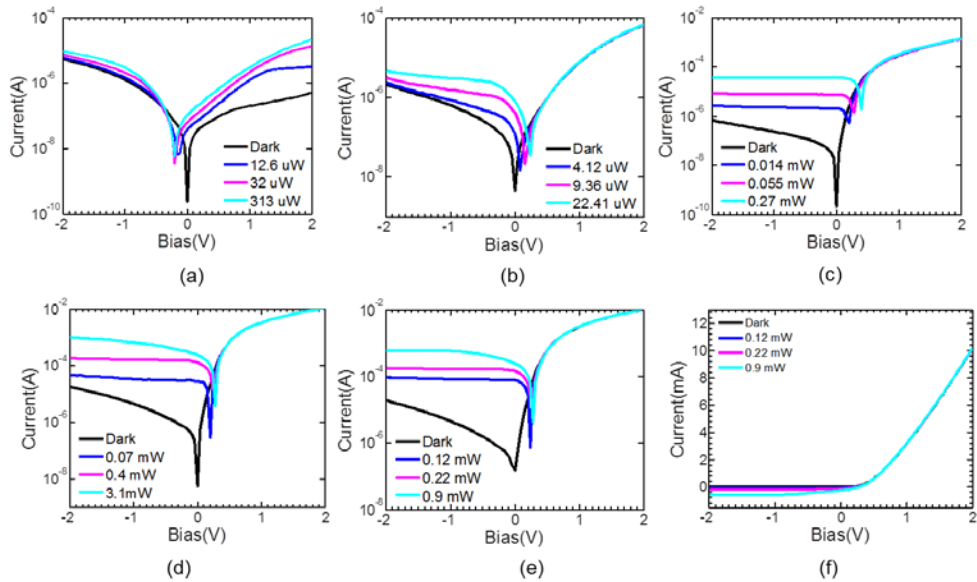
Figure 4-10 Measured responsivity of blue, green and red junctions of silicon under illumination with a) 405nm b)532nm c)632nm and InGaAs under illumination with d) 98nm and e) 1550nm wavelengths (f) linear graph of (e)

Figure 4-11 shows the response of the pixel junctions when they are illuminated with the corresponding wavelength and with white light. The response of a junction to the respective color is higher than the dark current, and the response to white light is higher than the dark current and response to the junction specific wavelength, since the intensity of white light is higher than other two parameters.
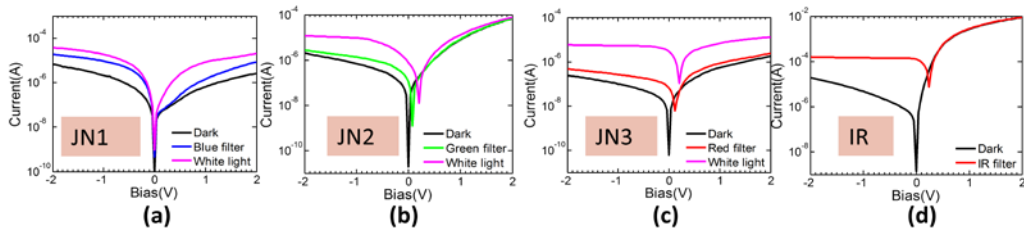
Figure 4-11 Photoresponse of Si and InGaAs PDs when illuminated (a)Response of junction 1 to white light and blue light (b)Response of junction 2 to white light and green light (c)Response of junction 3 to white light and red light (d)Response of InGaAs to IR wavelength

63

Figure 4-12 shows the response of the pixel junctions when they are not illuminated. As can be seen, there is no difference between the dark current and response to the junction specific wavelength. This is due to the fact that since the pixels are not illuminated, there is no photoresponse, hence the blue, green and red lines are synonymous with the black line, which represents dark current. This can be compared to the response when illuminated with white light, which is represented by the pink line.
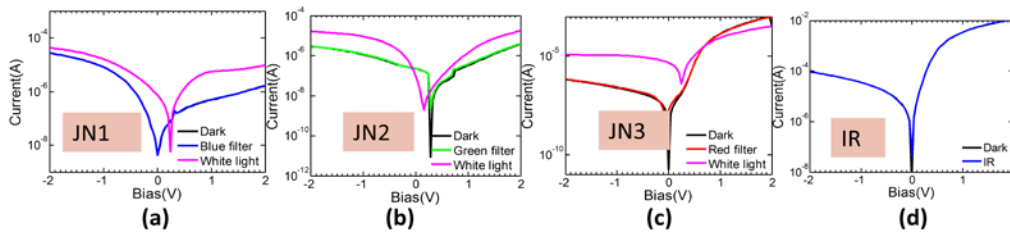
Figure 4-12 Photoresponse of Si and InGaAs PDs when non illuminated (a)Response of junction 1 to white light and blue light (b)Response of junction 2 to white light and green light (c)Response of junction 3 to white light and red light (d)Response of InGaAs to IR wavelength

Two important figures of merit for a photodetector, apart from responsivity are Noise Equivalent Power(NEP) and detectivity[79]. The Noise Equivalent Power (NEP) is the common metric that quantifies a photodetector's sensitivity or the power generated by a noise source. It is defined as the input signal power that results in a signal-to-noise ratio (S/R) of 1 in a 1 Hz output bandwidth. Essentially, the NEP expresses the minimum detectable power per square root bandwidth of a given detector; in other words, it's a measure of the weakest optical signal that can be detected. Detectivity is defined as the inverse of NEP. The values of NEP and detectivity for various wavelengths are shown in the table below.

Table 4.3 NEP and detectivity at various wavelengths

Bias (V)	NEP(W/√Hz)					Detectivity(√Hz/W)				
	405nm	532nm	632nm	980nm	1550nm	405nm	532nm	632nm	980nm	1550nm
0	7.41E-14	1.25E-14	4.51E-14	8.34E-14	1.17E-13	1.34E13	7.96E13	2.21E13	1.19E13	8.51E12
-2	8.20E-12	6.58E-12	6.80E-12	4.82E-12	3.01E-12	1.21E11	1.52E11	1.46E11	2.07E11	3.31E11

4.3.4 Characterization- Imaging

All the silicon and InGaAs detectors were tested individually for uniformity and the imaging performance was also analyzed. By measuring the spectral responsivities for each junction, color (spectral) information can be resolved based on post-imaging data process, which can be used to construct color images. Imaging was done using a QTH white light source that was focused on the 4x4 heterogeneous photodetector array through a narrow slit, wide enough to illuminate only one column of pixels in the 4x4 array. On the array, the pixels that are not illuminated by the light through the slit will remain dark. The resulting photoresponse of the 16 Si(Jn1,Jn2,Jn3) photodetectors and 16 InGaAs photodetectors are recorded. The resulting image formed after data handling is shown in Fig. 5, for the blue, green, red and IR junctions. The illuminated column (column 2 for blue junction, and column 3 for green red and IR junctions) can easily be distinguished from the non-illuminated columns. The horizontal and vertical numbers in the figure indicate the row and column number of the array. Each square in the figures represent the difference in the measured photo current and dark current for that specific junction of the pixel. The scale bar on the right side of each figure, shows the range of

values in the square. Non uniformity in color is due to the variation of this diference between the various pixels, for that specific junction , as the photoresponse of all the devices are not exactly the same. It is worth mentioning that due to the process variations, we observed better performance for the blue junctions from column 2, and better performance for other junctions from column 3. With further process optimization, it is possible to   obtain much better imagers with more uniform performance for all junctions/pixels. Most importantly, the junction isolation and planarization of multilayer polyimide process for multi-layer interconnects are major sources of process variations, which can be improved with well controlled processes for both thick photoresist patterning/alignment and patterning/curing of the multi-layer polyimide processes.
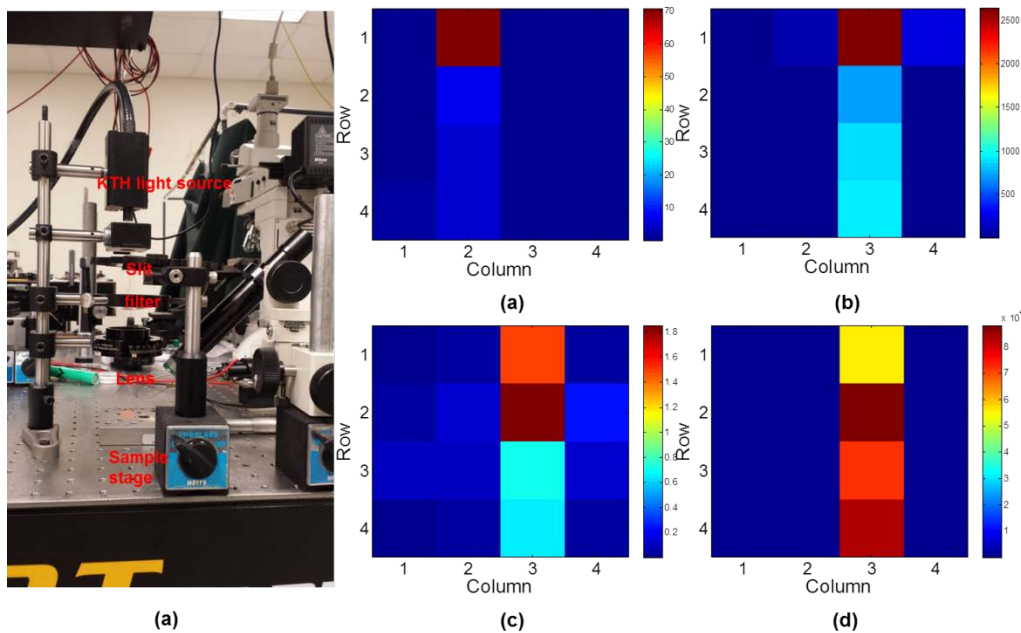
Figure 4-13 Imaging with the 4x4 array a) Imaging set up. Imaging a column of illuminated pixels in b) blue c) green d) red and e) IR junctions

Chapter 5

CONCULDING REMARKS AND FUTURE RESEARCH

In this thesis, various detector configurations are presented- Single InGaAs photodetector, InGaAs photodetector array on substrate, flexible InGaAs photodetector array (on kapton), Silicon photodetector array on substrate, flexible silicon photodetector array, vertically integrated silicon and InGaAs photodetector array, adjacently integrated silicon and InGaAs photodetector array. This thesis presents extensive fabrication process, device design, and device characterization.

Initially, fabrication of single InGaAs photodetector is presented, with the responsivity measurements. This paves the way for InGaAs photodetector array. An 8x8 InGaAs PD array is demonstrated on InP substrate. The structure is a PIN, with 2µm InGaAs active layer. IV measurements for all the 64 InGaAs PDs and responsivity measurements with both 980nm and 1550 nm are presented. A linear relationship is observed between the input power and the output photocurrent. To extend the applications of the InGaAs array, flexible InGaAs PD array is presented. The InGaAs array is transferred to kapton substrate by the use of black wax and wet transfer. Characterization details with 980nm and 1550nm laser excitations are presented with a comparison between the InGaAs PD array response on InP substrate and on kapton substrate.

An 8x8 silicon multi-color PD array is designed on a n-p-n-p structure, to form a detector array that is capable of spectral separation and detection of red, blue and green colors. The thickness of each layer of the vertical structure is optimized to match the absorption depth of blue, green and red wavelengths in silicon. The fabrication process details are presented with imaging data. Moving a step further, the 8x8 Si PD array is also demonstrated on a flexible kapton substrate. The process of transfer printing using

67

an elastomer like PDMS is demonstrated in this Si array fabrication process. Characterization of this flexible PD array is performed by IV measurements and imaging. The responsivities of the first, second and third P-N junction, for the detection of blue, green and red colors are 0.1 A/W, 0.09 A/W and 0.07 A/W respectively. The measured values are in good agreement with the values predicted by Medici simulation. Array performance is evaluated by measuring the uniformity of all the 64 pixels in the array and by imaging. By using a QTH light source, illuminating the array through a hard mask, the capability of the SI PD array to detect and recreate the letter "H" is demonstrated. Flexibility of this array is investigated by performing bending tests. IV measurements before and during the bending proves that there is no performance degradation due to bending, and the response of the PD array remains the same in a bent state.

Heterogeneously integrated detectors are appealing to do the wide range of wavelengths they can detect, beyond the capability of the individual detectors/materials. To achieve a broad detection in visible and Near –IR (NIR) range, two different configuration of integration of silicon and InGaAs are explored. First configuration is vertically integrated Silicon on InGaAs 8x8 array structure. A 2 µm active Si layer, pre-doped to form a P-N junction, is transferred on the surface of a PIN InGaAs structure by PDMS transfer printing process. This heterogeneously integrated structure is experimentally demonstrated and characterized. Si performance is analyzed with 405nm laser and InGaAs, with 1550nm laser. IV test results prove excellent isolation between the silicon and InGaAs detection.

Second configuration is adjacent placement of Si and InGaAs in a 4x4 array layout. The intricacies of the device fabrication are explored in detail, with the introduction of a novel aligner-assisted PDMS transfer printing process. This method solves the problem of perfect alignment during transfer of unconnected Si mesas from SOI substrate

68

to InGaAs substrate that normally occurs during hand transfer. The SOI used in this process has a 6μm active Si layer with a n-p-n-p doping profile and the InGaAs substrate is a PIN structure with a 2 μm I layer. The device array consists of 4x4 Si PDs and 4x4 InGaAs PDs adjacently placed next to each other. Individual Si and InGaAs pixels are characterized with 405 nm, 532 nm and 632nm lasers for Si and 980 nm and 1550nm lasers for InGaAs. The responsivities of the Si PD for the first, second and third junctions are demonstrated to be 0.09 A/W, 0.1 A/W and 0.15 A/W respectively and the responsivity of the InGaAs PD for 980nm and 1550nm laser excitation is proven to be 0.5 A/W and 0.8 A/W. These values of responsivities are shown to be in good agreement with the simulated values.

Appendix A

List of Publications

Journal Publications

1.   **Laxmy Menon**, Hongjun Yang, Sang June Cho, Solomon Mikael, Zhenqiang Ma, and Weidong Zhou, "Transferred Flexible Three-Color Silicon Membrane Photodetector Arrays", *IEEE Photon. J.* 7, (1), 6800106 (2015)

2.   **Laxmy Menon**, Hongjun Yang, Sang June Cho, Solomon Mikael, Zhenqiang Ma, and Weidong Zhou, "Heterogeneously Integrated InGaAs and Si Membrane Four Color Focal Plane Arrays", *IEEE Photon. J.*.Accepted

3.   Yonghao Liu, Arvinder Chadha, Deyin Zhao, Jessica R. Piper, Yichen Jia, Yichen Shuai, **Laxmy Menon**, Hongjun Yang, Zhenqiang Ma, Shanhui Fan, Fengnian Xia and W. Zhou, "Approaching total absorption at near infrared in a large area monolayer graphene by critical coupling", *Appl. Phys. Lett.* 105, 181105 (2014)

4.   **Laxmy Menon**, Hongjun Yang, Zhenqiang Ma, Mattias Hammar, Weidong Zhou, "Heterogeneous integration of Si and InGaAs photodetector arrays for multi-band detection" Compound Semiconductor magazine, June issue

5.   W. Fan, T Chang, S.C. Liu, , **L.Menon**, H. Yang, J.Berggren, M. Hammar, Z.Ma, W. Zhou, "Selective Release of InP Heterostructures from InP Substrates " Submitted.

6.   **Laxmy Menon**, Hongjun Yang "Transfer process for unconnected mesas" TBP.

CONFERENCES

1.   "Flexible three color silicon membrane photodetector arrays", **L.Menon**, H.Yang, J.H.Seo,S.Wang, Z.Ma, W.Zhou, IEEE photonics Conference, San Diego,CA, Oct 12-18,2014

2.   "Transfer printing for heterogeneously integrated multi-color imagers and graphene-photonic crystal cavities", **L.Menon**, H.Yang,, Y. Liu, D.Zhao, Z. Ma, W. Zhou, IPC Summer Topicals, Nassau, Bahamas, July 12-15, 2015.

3.   "Heterogeneously integrated InGaAs and Si membrane four color focal plane arrays", **L.Menon,** H.Yang, SJ Cho, S. Mikael, Z.Ma, W.Zhou, IEEE photonics Conference, Reston,VA , Oct 4-8,2015.

4.   "Flexible visible/IR multiband membrane imager array", **L.Menon**, H.Yang, SJ Cho, S. Mikael, Z.Ma, W.Zhou,UTA photonics Symposium, Arlington, TX , Sept 14, 2015.

References

[1]   W. Herschel, "Experiments on the Refrangibility of the Invisible Rays of the Sun. By William Herschel, LL. DFRS," *Philosophical Transactions of the Royal Society of London,* vol. 90, pp. 284-292, 1800.

[2]   E. S. Barr, "The Infrared Pioneers—III. Samuel Pierpont Langley," *Infrared physics,* vol. 3, pp. 195-206, 1963.

[3]   M. Razeghi, D. Hoffman, B.-M. Nguyen, P.-Y. Delaunay, E. K.-w. Huang, M. Z. Tidrow*, et al.*, "Recent advances in LWIR Type-II InAs/GaSb superlattice photodetectors and focal plane arrays at the center for quantum devices," *Proceedings of the IEEE,* vol. 97, pp. 1056-1066, 2009.

[4]   S. Krishna, "Quantum dots-in-a-well infrared photodetectors," *Infrared physics & technology,* vol. 47, pp. 153-163, 2005.

[5]   A. Rogalski, "Infrared detectors: status and trends," *Progress in quantum electronics,* vol. 27, pp. 59-210, 2003.

[6]   E. Towe and D. Pan, "Semiconductor quantum-dot nanostructures: their application in a new class of infrared photodetectors," *Selected Topics in Quantum Electronics, IEEE Journal of,* vol. 6, pp. 408-421, 2000.

[7]   V. I. Stafeev, "Mercury cadmium telluride: main semiconductor material of modern IR photoelectronics," in *XVI International Conference on Photoelectronics and Night Vision Devices*, 2000, pp. 240-243.

[8]   J. Wang, X. Chen, W. Hu, L. Wang, W. Lu, F. Xu*, et al.*, "Amorphous HgCdTe infrared photoconductive detector with high detectivity above 200 K," *Applied Physics Letters,* vol. 99, p. 113508, 2011.

[9]   C. Besikci, "III-V infrared detectors on Si substrates," in *Symposium on Integrated Optoelectronics*, 2000, pp. 31-39.

[10]   A. Rogalski, "Optical detectors for focal plane arrays," *Optoelectronics review,* vol. 12, pp. 221-246, 2004.

[11]   T. Martin, R. Brubaker, P. Dixon, M.-A. Gagliardi, and T. Sudol, "640x512 InGaAs focal plane array camera for visible and SWIR imaging," in *Defense and Security*, 2005, pp. 12-20.

[12]   B. M. Onat, W. Huang, N. Masaun, M. Lange, M. H. Ettenberg, and C. Dries, "Ultra-low dark current InGaAs technology for focal plane arrays for low-light level visible-shortwave infrared imaging," in *Defense and Security Symposium*, 2007, pp. 65420L-65420L-9.

[13]   H. Yuan, M. Meixell, J. Zhang, P. Bey, J. Kimchi, and L. C. Kilmer, "Low dark current small pixel large format InGaAs 2D photodetector array development at Teledyne Judson Technologies," in *SPIE Defense, Security, and Sensing*, 2012, pp. 835309-835309-8.

[14]   P. A. Scowen, S. Nikzad, M. Hoenk, I. Gontijo, A. Shapiro, F. Greer*, et al.*, "Large Focal Plane Arrays for Future Missions," *arXiv preprint arXiv:0904.1991,* 2009.

[15]   M. J. Cohen, M. H. Ettenberg, M. J. Lange, and G. H. Olsen, "An Indium Gallium Arsenide Visible/SWIR Focal Plane Array for Low Light Level Imaging," DTIC Document1999.

[16]   M. D. Enriquez, M. A. Blessinger, J. V. Groppe, T. M. Sudol, J. Battaglia, J. Passe*, et al.*, "Performance of high resolution visible-InGaAs imager for day/night vision," in *SPIE Defense and Security Symposium*, 2008, pp. 69400O-69400O-9.

[17]   M. J. Nelson, M. F. Skrutskie, S. Kanneganti, and C. Park, "High sensitivity infrared extended wavelength response InGaAs detectors," in *SPIE Astronomical Telescopes+ Instrumentation*, 2008, pp. 702122-702122-9.

[18]   A. Hoffman, T. Sessler, J. Rosbeck, D. Acton, and M. Ettenberg, "Megapixel InGaAs arrays for low background applications," in *Defense and Security*, 2005, pp. 32-38.

[19]   M. MacDougal, J. Geske, C. Wang, S. Liao, J. Getty, and A. Holmes, "Low dark current InGaAs detector arrays for night vision and astronomy," in *SPIE Defense, Security, and Sensing*, 2009, pp. 72983F-72983F-10.

[20]   J. B. Barton, R. F. Cannata, and S. M. Petronio, "InGaAs NIR focal plane arrays for imaging and DWDM applications," in *AeroSense 2002*, 2002, pp. 37-47.

[21]   C. Skrimshire, J. Farr, D. Sloan, M. Robertson, P. Putland, J. Stokoe*, et al.*, "Reliability of mesa and planar InGaAs PIN photodiodes," in *Optoelectronics, IEE Proceedings J*, 1990, pp. 74-78.

[22]   H. Temkin, R. Frahm, N. Olsson, C. Burrus, and R. McCoy, "Very high speed operation of planar InGaAs/InP photodiode detectors," *Electronics Letters,* vol. 22, pp. 1267-1269, 1986.

[23]   V. Andrievski and S. Malyshev, "High speed InGaAs photodetector modules for fibre optic communications," in *High Performance Electron Devices for Microwave and Optoelectronic Applications, 1997. EDMO. 1997 Workshop on*, 1997, pp. 335-339.

[24]   Y.-L. Lee, C.-C. Huang, C.-L. Ho, and M.-C. Wu, "Planar InGaAs pin photodiodes with transparent-conducting-based antireflection and double-path reflector," *Electron Device Letters, IEEE,* vol. 34, pp. 1406-1408, 2013.

[25]   Y. Wang, S.-J. Chang, C. Tsai, M.-C. Wu, Y.-Z. Chiou, S. Chang*, et al.*, "10-Gb/s planar InGaAs pin photodetectors," *Sensors Journal, IEEE,* vol. 10, pp. 1559-1563, 2010.

[26]   T. Lee, C. Burrus, A. Dentai, and K. Ogawa, "Small area InGaAs/InP pin photodiodes: fabrication, characteristics and performance of devices in 274 Mb/s and 45 Mb/s lightwave receivers at 1.31 Â¿ m wavelength," *Electronics Letters,* vol. 16, pp. 155-156, 1980.

[27]   G. Olsen, "Low-leakage, high-efficiency, reliable VPE InGaAs 1.0-1.7 µm photodiodes," *Electron Device Letters, IEEE,* vol. 2, pp. 217-219, 1981.

[28]   J. E. Bowers, C. Burrus, and R. McCoy, "InGaAs PIN photodetectors with modulation response to millimetre wavelengths," *Electronics Letters,* vol. 21, pp. 812-814, 1985.

[29]   K. Ohnaka, M. Kubo, and J. Shibata, "A low dark current InGaAs/InP pin photodiode with covered mesa structure," *Electron Devices, IEEE Transactions on,* vol. 34, pp. 199-204, 1987.

[30]   C. Downs and T. Vandervelde, "Progress in infrared photodetectors since 2000," *Sensors (Basel, Switzerland),* vol. 13, pp. 5054-5098, 2012.

[31]   P. L. Dillon, A. T. Brault, J. R. Horak, E. Garcia, T. W. Martin, and W. A. Light, "Fabrication and performance of color filter arrays for solid-state imagers," *Solid-State Circuits, IEEE Journal of,* vol. 13, pp. 23-27, 1978.

[32]   K. A. Parulski, "Color filters and processing alternatives for one-chip cameras," *Electron Devices, IEEE Transactions on,* vol. 32, pp. 1381-1389, 1985.

[33]   Q. Zhu, S. Coors, B. Schneider, P. Rieve, and M. Böhm, "Bias sensitive a-Si (C): H multispectral detectors," *Electron Devices, IEEE Transactions on,* vol. 45, pp. 1393-1398, 1998.

[34] G. De Cesare, F. Irrera, F. Lemmi, and F. Palma, "Amorphous Si/SiC three-color detector with adjustable threshold," *Applied physics letters,* vol. 66, pp. 1178-1180, 1995.

[35] J. Dresner, "Amorphous silicon p-i-n-i-p and n-i-p-i-n diodes," *Applied physics letters,* vol. 48, pp. 1006-1008, 1986.

[36] D. Knipp, H. Stiebig, J. Fölsch, F. Finger, and H. Wagner, "Amorphous silicon based nipiin structure for color detection," *Journal of applied physics,* vol. 83, pp. 1463-1468, 1998.

[37] M. Tucci, R. De Rosa, F. Roca, D. Caputo, and G. de Cesare, "Amorphous silicon p–i–n on p crystalline silicon photodetector in the visible and near infrared spectrum," *Journal of Non-Crystalline Solids,* vol. 266, pp. 1218-1222, 2000.

[38] J. Zimmer, D. Knipp, H. Stiebig, and H. Wagner, "Amorphous silicon-based unipolar detector for color recognition," *Electron Devices, IEEE Transactions on,* vol. 46, pp. 884-891, 1999.

[39] M. Topic, H. Stiebig, D. Knipp, and F. Smole, "Optimization of a-Si: H-based three-terminal three-color detectors," *Electron Devices, IEEE Transactions on,* vol. 46, pp. 1839-1845, 1999.

[40] H. Lee, T. Suh, B. Choe, K. Shinn, G. Cho, and V. Perez-Mendez, "Transient photoconductive gain in a-Si: H devices and its applications in radiation detection," *Nuclear Instruments and Methods in Physics Research Section A: Accelerators, Spectrometers, Detectors and Associated Equipment,* vol. 399, pp. 324-334, 1997.

[41] R. F. Lyon and P. M. Hubel, "Eyeing the camera: Into the next century," in *Color and Imaging Conference*, 2002, pp. 349-355.

[42] D. Knipp, H. Stiebig, J. Fölsch, and H. Wagner, "Four terminal color detector for digital signal processing," *J. Non-Cryst. Solids* vol. 227, pp. 1321-1325, 1998.

[43] P. M. Hubel, J. Liu, and R. J. Guttosch, "Spatial frequency response of color image sensors: Bayer color filters and Foveon X3," in *Electronic Imaging 2004*, 2004, pp. 402-407.

[44] D. L. Gilblom, S. K. Yoo, and P. Ventura, "Real-time color imaging with a CMOS sensor having stacked photodiodes," in *Optical Science and Technology, SPIE's 48th Annual Meeting*, 2004, pp. 105-115.

[45] D. L. Gilblom, S. K. Yoo, and P. Ventura, "Operation and performance of a color image sensor with layered photodiodes," in *AeroSense 2003*, 2003, pp. 318-331.

[46] P. M. Hubel, "Foveon technology and the changing landscape of digital cameras," in *Color and Imaging Conference*, 2005, pp. 314-317.

[47] D. Knipp, R. A. Street, H. Stiebig, M. Krause, J.-P. Lu, S. Ready*, et al.*, "Vertically integrated thin film color sensor arrays for imaging applications," *Optics express,* vol. 14, pp. 3106-3113, 2006.

[48] P. Dixit and J. Miao, "Effect of SF6 flow rate on the etched surface profile and bottom grass formation in deep reactive ion etching process," in *Journal of Physics: Conference Series*, 2006, p. 577.

[49] M. A. Meitl, Z.-T. Zhu, V. Kumar, K. J. Lee, X. Feng, Y. Y. Huang*, et al.*, "Transfer printing by kinetic control of adhesion to an elastomeric stamp," *Nature Mat.,* vol. 5, pp. 33-38, 2005.

[50] W. Zhou, D. Zhao, Y.-C. Shuai, H. Yang, S. Chuwongin, A. Chadha*, et al.*, "Progress in 2D photonic crystal Fano resonance photonics," *Progress in Quantum Electronics,* vol. 38, pp. 1-74, 2014.

[51]   S. I. Park, J. H. Ahn, X. Feng, S. Wang, Y. Huang, and J. A. Rogers, "Theoretical and experimental studies of bending of inorganic electronic materials on plastic substrates," *Advanced Functional Materials,* vol. 18, pp. 2673-2684, 2008.

[52]   D. Hertel, H. Marechal, D. Tefera, W. Fan, and R. Hicks, "A low-cost VIS-NIR true color night vision video system based on a wide dynamic range CMOS imager," in *Intelligent Vehicles Symposium, 2009 IEEE*, 2009, pp. 273-278.

[53]   V. Tsagaris and V. Anastassopoulos, "Fusion of visible and infrared imagery for night color vision," *Displays,* vol. 26, pp. 191-196, 2005.

[54]   A. M. Waxman, A. N. Gove, D. A. Fay, J. P. Racamato, J. E. Carrick, M. C. Seibert*, et al.*, "Color night vision: opponent processing in the fusion of visible and IR imagery," *Neural Networks,* vol. 10, pp. 1-6, 1997.

[55]   J.-H. Lyu, S. Choi, J. H. Choi, J. H. Nam, and J. B. Jung, "IR/Color Composite Image Sensor with VIPS (Vertically Integrated Photodiode Structure)," in *International Image Sensor Workshop*, 2007, pp. 7-10.

[56]   G. Langfelder, "CMOS pixels directly sensitive to both visible and near-infrared radiation," *IEEE Trans. Electron Devices,* vol. 60, pp. 1695-1700, 2013.

[57]   N. Papanicolaou, G. Anderson, A. Iliadis, and A. Christou, "Lattice mismatched InGaAs on silicon photodetectors grown by molecular beam epitaxy," *Journal of electronic materials,* vol. 22, pp. 201-206, 1993.

[58]   E. Peiner, A. Guttzeit, and H.-H. Wehmann, "The effect of threading dislocations on optical absorption and electron scattering in strongly mismatched heteroepitaxial III–V compound semiconductors on silicon," *Journal of Physics: Condensed Matter,* vol. 14, p. 13195, 2002.

[59]   Y. B. Bolkhovityanov and O. P. Pchelyakov, "GaAs epitaxy on Si substrates: modern status of research and engineering," *Physics-Uspekhi,* vol. 51, pp. 437-456, 2008.

[60]   S. Fang, K. Adomi, S. Iyer, H. Morkoc, H. Zabel, C. Choi*, et al.*, "Gallium arsenide and other compound semiconductors on silicon," *Journal of Applied Physics,* vol. 68, pp. R31-R58, 1990.

[61]   Y. Gao, Z. Zhong, S. Feng, Y. Geng, H. Liang, A. W. Poon*, et al.*, "High-speed normal-incidence pin InGaAs photodetectors grown on silicon substrates by MOCVD," *Photonics Technology Letters, IEEE,* vol. 24, pp. 237-239, 2012.

[62]   A. Katsnelson, V. E. Tokranov, M. Yakimov, M. Lamberti, and S. Oktyabrsky, "Hybrid integration of III-V optoelectronic devices on Si platform using BCB," in *Integrated Optoelectronics Devices*, 2003, pp. 198-205.

[63]   U. Christiaens, G. Roelkens, K. De Mesel, and D. Van, "Adhesive wafer bonding with Benzocyclobutene," *IEEE JOURNAL OF LIGHTWAVE TECHNOLOGY,* vol. 1, 2004.

[64]   J. Brouckaert, G. Roelkens, D. Van Thourhout, and R. Baets, "Thin-film III–V photodetectors integrated on silicon-on-insulator photonic ICs," *Journal of Lightwave Technology,* vol. 25, pp. 1053-1060, 2007.

[65]   D. Pasquariello, M. Camacho, and K. Hjort, "Low temperature epitaxial layer transferring using oxygen plasma wafer bonding," in *Lasers and Electro-Optics Society 2000 Annual Meeting. LEOS 2000. 13th Annual Meeting. IEEE*, 2000, pp. 852-853.

[66]   D. Liang and J. Bowers, "Highly efficient vertical outgassing channels for low-temperature InP-to-silicon direct wafer bonding on the silicon-on-insulator substrate," *Journal of Vacuum Science & Technology B,* vol. 26, pp. 1560-1568, 2008.

[67] Q.-Y. Tong and U. M. Gösele, "Wafer bonding and layer splitting for microsystems," *Advanced Materials,* vol. 11, pp. 1409-1425, 1999.

[68] C. Monat, C. Seassal, X. Letartre, P. Viktorovitch, P. Regreny, M. Gendry*, et al.*, "InP 2D photonic crystal microlasers on silicon wafer: room temperature operation at 1.55 µm," *Electronics Letters,* vol. 37, p. 1, 2001.

[69] D. Pasquariello and K. Hjort, "Plasma-assisted InP-to-Si low temperature wafer bonding," *Selected Topics in Quantum Electronics, IEEE Journal of,* vol. 8, pp. 118-131, 2002.

[70] T. Akatsu, A. Plößl, R. Scholz, H. Stenzel, and U. Gösele, "Wafer bonding of different III–V compound semiconductors by atomic hydrogen surface cleaning," *Journal of Applied Physics,* vol. 90, pp. 3856-3862, 2001.

[71] V. Dragoi, T. Glinsner, G. Mittendorfer, B. Wieder, and P. Lindner, "Adhesive wafer bonding for MEMS applications," in *Microtechnologies for the New Millennium 2003*, 2003, pp. 160-167.

[72] F. Niklaus, P. Enoksson, E. Kälvesten, and G. Stemme, "Low-temperature full wafer adhesive bonding," *Journal of Micromechanics and Microengineering,* vol. 11, p. 100, 2001.

[73] J.-H. Ahn, H.-S. Kim, K. J. Lee, S. Jeon, S. J. Kang, Y. Sun*, et al.*, "Heterogeneous three-dimensional electronics by use of printed semiconductor nanomaterials," *science,* vol. 314, pp. 1754-1757, 2006.

[74] F. N. Ishikawa, H.-k. Chang, K. Ryu, P.-c. Chen, A. Badmaev, L. Gomez De Arco*, et al.*, "Transparent electronics based on transfer printed aligned carbon nanotubes on rigid and flexible substrates," *ACS nano,* vol. 3, pp. 73-79, 2008.

[75] L. Menon, H. Yang, S. J. Cho, S. Mikae, Z. Ma, and W. Zhou, "Transferred Flexible Three-Color Silicon Membrane Photodetector Arrays," *IEEE Photonics J.,* vol. 7, pp. 1-6, 2015.

[76] W. Zhou, Z. Ma, H. Yang, Z. Qiang, G. Qin, H. Pang*, et al.*, "Flexible photonic-crystal Fano filters based on transferred semiconductor nanomembranes," *Journal of Physics D: Applied Physics,* vol. 42, p. 234007, 2009.

[77] L. Sun, G. Qin, J. H. Seo, G. K. Celler, W. Zhou, and Z. Ma, "12-GHz Thin-Film Transistors on Transferrable Silicon Nanomembranes for High-Performance Flexible Electronics," *Small,* vol. 6, pp. 2553-2557, 2010.

[78] K. Zhang, J.-H. Seo, W. Zhou, and Z. Ma, "Fast flexible electronics using transferrable silicon nanomembranes," *Journal of Physics D: Applied Physics,* vol. 45, p. 143001, 2012.

[79] F. Perry, "Predicting the performance of a photodetector."

Biographical Information

Laxmy was born in Kerala, India. She received her Bachelor of Engineering degree from University of Madras, specializing in electronics and instrumentation. In 2005, she obtained her Masters degree in Electrical Engineering from University of Texas, Arlington. Her focus was on semiconductor devices and MEMS.

In Fall 2010, Laxmy joined Dr. Weidong Zhou's Nanophotonics group at University of Texas at Arlington as a PhD candidate. Her research interests include design, fabrication and characterization of III-V photodetectors, Si photodetectors and heterogeneous integration of dissimilar materials to obtain photodetection in a wide spectrum. She has worked on VCSELS and 2D materials, with an emphasis on fabrication of active devices with these materials. She has also worked on Raman spectroscopy as a means to monitor wound healing by integrating state-of-art nanophotonic membrane device technology, robust fluorescent and surface enhanced Raman scattering (SERS) signals of dye and metal nanoparticles, and smart shape memory polymer materials.

Laxmy's research interests include applied aspects of nanofabrication for rigid and flexible photonic and optoelectronic devices. Laxmy plans to pursue a career on nanofabrication and development of novel and unusual optoelectronic devices.